Title:

Reduced Thalamic Excitation to Motor Cortical Pyramidal Tract Neurons in a Mouse Model of Parkinsonism

Liqiang Chen[1], Samuel Daniels[1], Rachel Dvorak[1], and Hong-Yuan Chu[1,*]

[1]Department of Neurodegenerative Science, Van Andel Research Institute, Grand Rapids, MI 49503 USA

[*]Corresponding author: Hong-Yuan Chu, Ph.D.

Address: 333 Bostwick Ave NE, Grand Rapids, MI 49503

Email: hongyuan.chu@vai.org

Phone: 616-234-5847

Author contribution: Investigation, formal analysis: L.C., S.D., R.D., and H.Y.C.; Conceptualization, funding acquisition, project administration, resources, supervision, visualization, writing – original draft: H.Y.C.; Writing – review& editing: L.C., S.D., and H.Y.C.

Competing interests: The authors declare no competing interests.

Acknowledgement: The authors thank the Van Andel Research Institute optical imaging core for the advanced confocal microscope, and Van Andel Research Institute vivarium for animal husbandry. The authors thank all members of the Chu lab at Van Andel Research Institute for thoughtful discussions. Funding: This work was supported by the National Institute of Neurological Disorders and Stroke (grant#: R01NS121371).

Materials & Correspondence: Correspondence and material requests should be addressed to Dr. Hong-Yuan Chu

Abstract

Degeneration of midbrain dopaminergic (DA) neurons causes a reduced motor output from the primary motor cortex (M1), underlying the motor symptoms of Parkinson's disease (PD). However, cellular and circuitry mechanisms of M1 dysfunction in PD remain undefined. Using multidisciplinary approaches, we found that DA degeneration induces cell-subtype- and inputs-specific reduction of thalamic excitation to M1 pyramidal tract (PT) neurons. Physiological and anatomical analyses suggest that DA degeneration induces a loss of thalamocortical synapses to M1 PT neurons, resulting in an impaired thalamic driving of their activities. Moreover, we showed that the decreased thalamocortical connectivity are mediated by an excessive activation of NMDA receptors of M1 PT neurons. Further, the decreased thalamocortical transmission in parkinsonism can be rescued by chemogenetically suppressing basal ganglia outputs. Together, our data suggest that the reduced motor cortical outputs in parkinsonism are not only an immediate consequence of basal ganglia inhibition but also involves specific local circuitry adaptations within M1. This study reveals novel insight in the pathophysiology of parkinsonian motor deficits.

Introduction

Degeneration of dopaminergic (DA) neurons in the substantia nigra pars compacta (SNc) is one of featured pathology of Parkinson's disease (PD), which is causally linked with the parkinsonian motor deficits. Following the loss of the SNc DA neurons, both magnitude and timing of GABAergic outputs from the basal ganglia to downstream motor regions are robustly altered, which cause an abnormal suppression of the initiation and execution of movements in PD (Albin et al., 1989; Galvan and Wichmann, 2008; McGregor and Nelson, 2019). The thalamocortical network integrates basal ganglia information and sends motor commands to the motor areas in the brain stem and the spinal cord for movement execution, placing it an ideal position to mediate many aspects of motor symptoms of PD, particularly those related to skilled motor activities.

The primary motor cortex (M1) plays a critical role in the acquisition and execution of skilled motor activity (Georgopoulos and Carpenter, 2015; Guo et al., 2015a; Shenoy et al., 2012). M1 sends temporal patterns of activity for the generation and execution of movements and such network dynamics depends on both intrinsic mechanisms and synaptic inputs (e.g., thalamic excitation) (Sauerbrei et al., 2020; Shenoy et al., 2012). In parkinsonian state, the pathological signals of the basal ganglia are predicted to decrease M1 output and/or disrupt its network dynamics, contributing to the manifestation of the hypokinetic symptoms in PD (Aeed et al., 2021; Brazhnik et al., 2016; Hyland et al., 2019; McGregor and Nelson, 2019). However, our understanding of M1 pathophysiology in parkinsonism remains incomplete.

72 A large body of evidence in literature suggests M1 circuitry dysfunction in
73 parkinsonism. Degeneration of SNc DA neurons impairs motor skills and decreases
74 forelimb representation in the M1 of rodents (Brown et al., 2009; Plowman et al., 2011;
75 Viaro et al., 2011), which perhaps involve intrinsic and synaptic adaptations in M1
76 associated with DA depletion (Aeed et al., 2021; Cousineau et al., 2020; Guo et al.,
77 2015b; Villalba et al., 2021). Consistently, M1 pyramidal neurons exhibit enhanced
78 bursting pattern of activity and synchronization following chronic DA degeneration (Aeed
79 et al., 2021; Goldberg et al., 2002; Pasquereau and Turner, 2011; Pasquereau et al.,
80 2016). For example, in MPTP-treated nonhuman primates (NHP), while the layer 5
81 pyramidal tract (PT) neurons exhibit a decreased rate and enhanced bursting pattern of
82 activity, the intratalencephalic (IT) neurons are largely intact (Pasquereau and Turner,
83 2011). In addition, both electrophysiology and optical imaging studies suggest an
84 impaired timing of PT neuronal activation and the execution of movement in
85 parkinsonian NHP and rodents (Aeed et al., 2021; Pasquereau et al., 2016). In
86 agreement with the earlier studies, our recent work reported that the PT, but not the IT,
87 neurons in M1 show selective reduction in their intrinsic excitability, and that such
88 intrinsic adaptations involve a combination of several ionic conductance (Chen et al.,
89 2021). Therefore, in addition to the acute effects of the abnormal basal ganglia
90 GABAergic inhibition, M1 circuits exhibit local adaptations at the cellular and synaptic
91 levels, which can be important aspects of the pathophysiology of motor deficit in PD.
92 Neural circuits are equipped with a variety of homeostatic synaptic plasticity
93 mechanisms to stabilize network function in face of perturbations (Turrigiano, 2011). For
94 example, our recent work demonstrated several synaptic and intrinsic adaptations in the

basal ganglia associated with pathological neuronal activity and DA degeneration (Chu et al., 2017; McIver et al., 2019). Based on the abnormal rate and pattern of M1 neuronal activity in parkinsonism, we hypothesized that loss of DA neurons induces cell-subtype- and input-specific synaptic adaptations of the glutamatergic inputs of M1 and that such synaptic adaptations contribute to the reduced cortical output in parkinsonism. A multidisciplinary approach was used to test these hypotheses in a well-established neurotoxin-based mouse model of parkinsonism.

Results

Mice received either 6-OHDA injections into the medial forebrain bundle (MFB) to induce the degeneration of SNc DA neurons ("6-OHDA mice" hereafter), or vehicle injections into the MFB as controls ("controls" hereafter). All physiology and anatomical studies were conducted between 3–5 weeks post-injections. To confirm a complete degeneration of nigrostriatal DA pathway in 6-OHDA mice, all animals were subject to behavioral tests at 3 weeks post-surgery, prior to electrophysiology and anatomy studies (Chen et al., 2021). Relative to controls, 6-OHDA mice showed a significant reduction of locomotor activity in open field test (distance travelled in 10 min, control = 39 [33–48] m, n = 51 mice; 6-OHDA = 21 [15–27] m, n = 52 mice; $p < 0.0001$, MWU test). Moreover, 6-OHDA mice also exhibited asymmetric forelimb use in cylinder test (% of ipsilateral forelimb use, controls = 50 [49–52]%, n = 51 mice; 6-OHDA = 85 [79–93]%, n = 52 mice; $p < 0.0001$, MWU test). *Post hoc* immunostaining of striatal TH was conducted, which showed a > 80% loss of nigrostriatal axon terminals in the lesioned hemisphere of 6-OHDA mice (%striatal $TH_{ipsilateral\ /contralateral\ TH}$, control = 100 [97–102]%, n = 51 mice; 6-OHDA = 11 [7–16]%, n = 52 mice; $p < 0.0001$, MWU test).

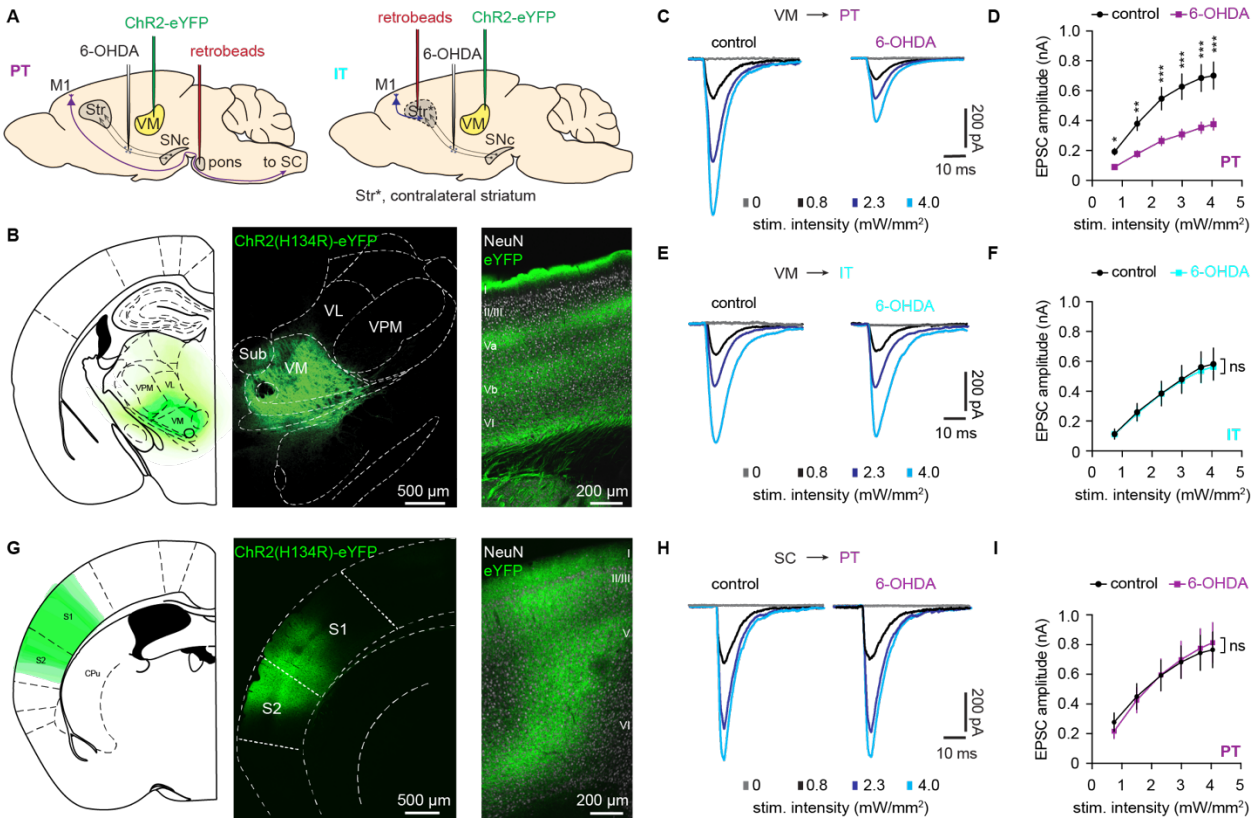

Figure 1. SNc DA degeneration induces cell-subtype- and input-specific alterations in M1. **A**) Schematic of overall strategies to retrogradely label M1 pyramidal neurons based on their projections and AAV-mediated optogenetics to selectively activate thalamocortical transmission arising from the ventromedial (VM) subregions of the motor thalamus of both controls and 6-OHDA mice. **B**) AAV-infected thalamic regions were overlaid to show the center of AAV injections across animals (left) and representative confocal images showing AAV9-ChR2(H134R)-eYFP infusion site in the motor thalamus that was centered at the VM subregion (middle), and ChR2(H134R)-eYFP-expressing thalamic axon terminals in the M1, which concentrate in the layers I and V (right). **C-D**) Representative traces of optogenetically-evoked EPSCs across different stimulation intensities in PT neurons from both controls and 6-OHDA mice (**C**) and the summarized results (**D**). **E-F**) Representative traces of optogenetically-evoked EPSCs across different stimulation intensities in IT neurons from both controls and 6-OHDA mice (**E**) and the summarized results (**F**). **G**) AAV-infected cortical regions were overlaid to show the center of AAV injections across animals (left) and representative confocal images showing AAV9-ChR2(H134R)-eYFP infusion site in the motor thalamus that was centered at the sensory cortical areas (middle), and ChR2(H134R)-eYFP-expressing cortical axon terminals in the M1 (right). **H-I**) Representative traces of optogenetically-evoked EPSCs arising from the SC across different stimulation intensities in M1 PT neurons from both controls and 6-OHDA mice (**H**) and the summarized results (**I**). *, $p < 0.05$, **, $p < 0.01$, ***, $p < 0.001$, ns, not significant.

122 **SNc DA degeneration induces cell-subtype- and input-specific alterations in M1**
123 **circuits**

124 To interrogate synaptic properties of thalamocortical inputs to projection-defined
125 subtypes of M1 layer 5 (L5) pyramidal neurons in controls and 6-OHDA mice, (1) AAV9-
126 hSyn-ChR2(H134R)-eYFP were injected into the motor thalamus (centering at the
127 ventromedial (VM) subregion of thalamus, **Fig. 1B**); (2) Retrobeads were stereotaxically
128 injected into the ipsilateral pontine nuclei and contralateral striatum to label PT and IT
129 neurons, respectively (**Figure 1A**). Three weeks post-injection, intense eYFP labeled
130 fibers could be observed, particularly in the layers I and V of M1 (**Figure 1B**). Synaptic
131 strength of thalamic inputs to PT and IT neurons were compared using *ex vivo*
132 electrophysiology and optogenetics in slices from controls and 6-OHDA mice.

133 Whole-cell voltage-clamp recordings of excitatory postsynaptic currents (EPSCs)
134 were conducted in the presence of TTX (1 μM) and 4-AP (100 μM) to prevent the
135 recruitment of polysynaptic responses and facilitate presynaptic glutamate release from
136 thalamic axon terminals (Hooks et al., 2013; Petreanu et al., 2007). The amplitude of
137 optogenetically-evoked thalamic EPSCs (oEPSCs) in M1 PT neurons was greatly
138 reduced in slices from 6-OHDA mice relative to those from controls across a range of
139 stimulation intensities ($p < 0.0001$, 2-way ANOVA followed by Sidak's tests, **Figure 1C,**
140 **D**). In contrast, the amplitude of oEPSCs in the IT neurons was unaltered between
141 slices from 6-OHDA mice and controls ($p > 0.05$, 2-way ANOVA, **Figure 1E, F**). These
142 data suggest that chronic SNc DA degeneration selectively decreases synaptic strength
143 of the motor thalamic excitation to M1 PT neurons.

Cerebral cortical neurons are equipped with a battery of homeostatic mechanisms to scale-up or -down synaptic strength to compensate for external perturbations (Turrigiano, 2011). Thus, we examined whether loss of SNc DA neurons decreases global excitation to PT neurons through homeostatic plasticity processes, or selectively decreases thalamic inputs? To answer this question, AAV-hsyn-ChR2(H134R)-eYFP were injected into the sensory cortical (SC) regions (**Figure 1G**) and retrobeads were injected into pons of 6-OHDA mice and controls. Next, we compared the connection strength of sensory cortical inputs to M1 PT neurons of 6-OHDA mice and controls. The amplitude of oEPSCs from SC to PT neurons (SC-PT) was not altered in slices from 6-OHDA mice relative to controls (**Figure 1H, I**). These data suggest that DA degeneration likely selectively decrease thalamic excitation to M1 PT neurons. Together, chronic DA degeneration leads to cell-subtype- and input-specific adaptions in M1 local circuits.

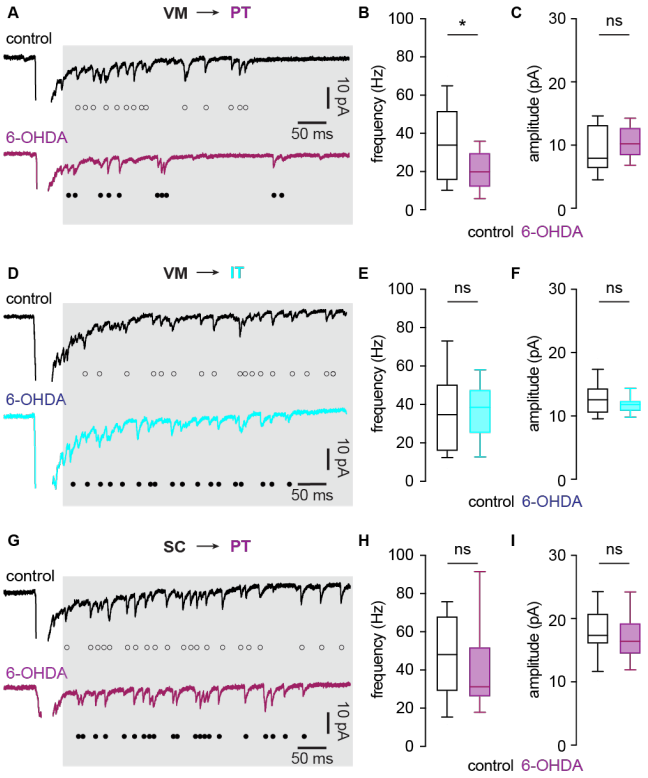

Figure 2. SNc DA degeneration decreases the number of functional thalamic inputs to M1 PT neurons. **A**) Representative traces showing optogenetically-evoked, Sr^{2+}-induced asynchronous thalamocortical EPSCs of PT neurons from controls and 6-OHDA mice. Open and filled circle indicate individual events of asynchronous EPSCs. **B-C**) Box plots showing a reduced frequency (B) and unaltered amplitude (C) of Sr^{2+}-EPSCs at thalamic inputs to M1 PT neurons from 6-OHDA mice relative to controls. **D**) Representative traces showing optogenetically-evoked, Sr^{2+}-induced quantal EPSCs of thalamic inputs to IT neurons from controls and 6-OHDA mice. Open and filled circle indicate individual events of asynchronous EPSCs. **E-F**) Box plots showing unaltered frequency (E) and amplitude (F) of Sr^{2+}-EPSCs at thalamic inputs to M1 IT neurons between groups. **G**) Representative traces showing optogenetically-evoked, Sr^{2+}-induced quantal EPSCs of sensory cortical inputs to PT neurons from controls and 6-OHDA mice. Open and filled circles indicate individual events of asynchronous EPSCs. **H-I**) Box plots showing unaltered frequency (H) and amplitude (I) of Sr^{2+}-EPSCs at sensory cortical inputs to M1 PT neurons between groups. *, $p < 0.05$, ns, not significant.

SNc DA degeneration decreases the number of functional thalamic inputs to M1 PT neurons

To gain mechanistic understanding of synaptic adaptations of M1 circuits following the loss of SNc DA neurons, we assessed the quantal properties of glutamatergic neurotransmission to PT and IT neurons in M1. Replacing extracellular Ca^{2+} with Sr^{2+} (2 mM), we found a significantly reduced frequency, but an unaltered amplitude, of optogenetically-evoked, Sr^{2+}-induced thalamic asynchronous EPSCs (Sr^{2+}-EPSCs) in the PT neurons from 6-OHDA mice relative to those from controls (frequency of Sr^{2+}-EPSCs, controls = 34 [15.5–52] Hz, n = 20 neurons/3 mice; 6-OHDA = 20 [12–30] Hz, n = 20 neurons/4 mice; $p = 0.02$, MWU; amplitude of Sr^{2+}-EPSCs, controls = 7.95 [6.3–13.2] pA, n = 20 neurons/3 mice; 6-OHDA = 10.2 [8.4–12.8] pA, n = 20 neurons/4 mice; $p = 0.33$, MWU, **Figure 2A-C**). In contrast, neither the frequency nor the amplitude of thalamic Sr^{2+}-EPSCs in the IT neurons was altered in 6-OHDA mice relative to controls

173 (frequency of Sr^{2+}-EPSCs, controls = 34.8 [15.7–50.5] Hz, n = 22 neurons/3 mice; 6-
174 OHDA = 38.4 [24.9–47.6] Hz, n = 22 neurons/3 mice; p = 0.7, MWU; amplitude of Sr^{2+}-
175 EPSCs, control = 12.6 [10.5–14.4] pA; 6-OHDA = 11.8 [10.8–12.4] pA; n = 22 neurons/3
176 mice; p = 0.34, MWU; **Figure 2D-F**). Consistent with the intact synaptic strength of
177 sensory cortical inputs to PT neurons (**Figure 1G-I**), the frequency and amplitude of
178 Sr^{2+}-EPSCs at SC–PT synapses were unaltered between groups (frequency of Sr^{2+}-
179 EPSCs, controls = 48 [29–68] Hz, n = 20 neurons/3 mice; 6-OHDA = 31.2 [26–52] Hz, n
180 = 19 neurons/3 mice; p = 0.6, MWU; amplitude of Sr^{2+}-EPSCs, control = 17 [16–20.8]
181 pA, n = 20 neurons/3 mice; 6-OHDA = 16.5 [14.4–19.3] pA, n = 19 neurons/3 mice; p =
182 0.5, MWU; **Figure 2G-I**). These data further support that SNc DA degeneration
183 selectively affect thalamic projection to PT neurons, largely due to fewer functional VM-
184 PT inputs.
185
186 **Loss of DA alters the structure of thalamocortical synapses to M1 PT neurons**
187 To assess how loss of DA alters thalamocortical innervation of M1 PT neurons, brain
188 sections from control and 6-OHDA mice were processed for immunohistochemical
189 detection of vesicular glutamate transporter 2 (vGluT2), a marker of thalamic axon
190 boutons in M1. Stereological methods were used to quantify vGluT2-immunoreactive
191 (vGluT2-ir) puncta in the layer V of M1. The density of vGluT2-ir puncta was significantly
192 decreased in slices from 6-OHDA mice relative to those from controls (control = 20.4
193 [16.9–22.9] million puncta/mm^3, n = 20 slices/3 mice; 6-OHDA = 11.2 [8.5–13.9] million
194 puncta/mm^3, n = 20 slices/3 mice; $p < 0.0001$, MWU; **Figure 3A-C**). These data are
195 consisted with findings from MPTP-treated NHP (Villalba et al., 2021). It has been

196 reported that reduced vGluTs levels per terminal leads to a smaller vesicle size (Wojcik

197 et al., 2004). Considering the unaltered quantal size of Sr^{2+}-EPSCs (**Figure 2A, C**), we

198 posit that the reduced vGluT2 density indicates a loss of presynaptic thalamic terminals,

199 rather than a decreased vGluT2 protein expression per thalamic axon terminal.

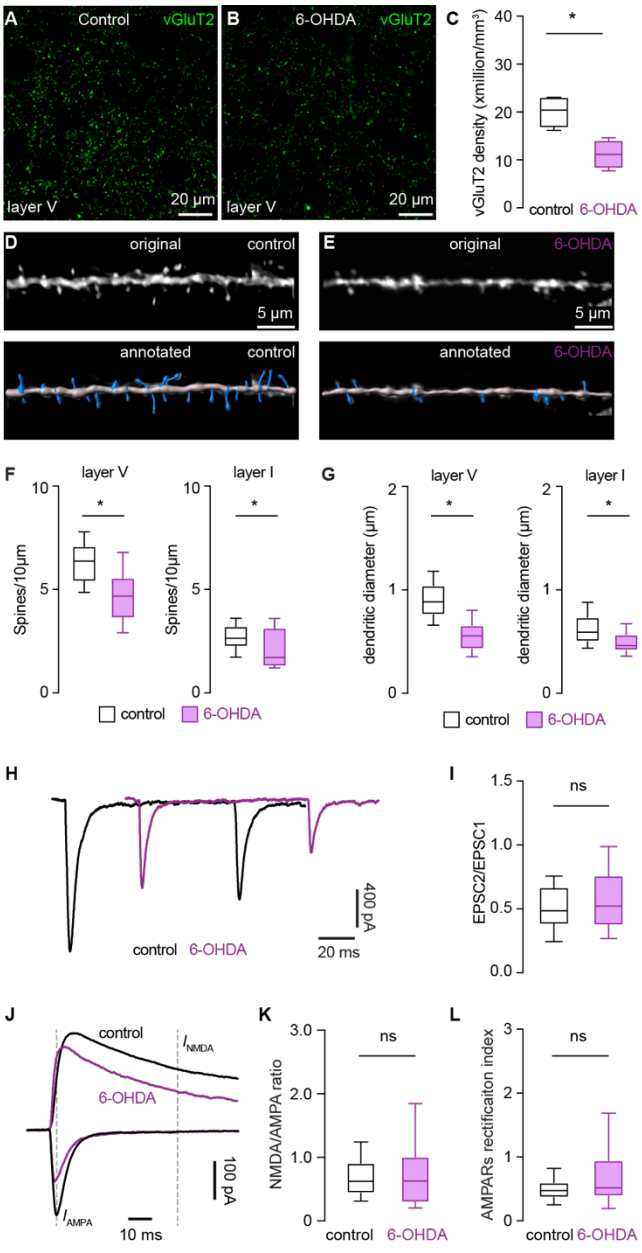

200

Figure 3. Degeneration of SNc DA neurons induces structural alterations of thalamocortical synapses. **A-C**) Representative confocal images of vGluT2-immunoreactivity in the layer 5 of M1 from controls (A) and 6-OHDA mice (B), and the summarized results showing a reduced vGluT2 density in the layer 5 of M1 following the SNc DA degeneration (**C**). **D-E**) Representative confocal images of segments of basal dendrites of M1 PT neurons from controls (D) and 6-OHDA mice (E). The bottom panels show the annotated dendrites using Imaris software. **F-G**) Summarized results showing decreased spine densities of L5 basal dendrites and L1 apical dendrites (F) and reduced dendritic diameters of L5 basal dendrites and L1 apical dendrites from 6-OHDA mice, relative to controls. **H-I**) Representative traces of EPSCs in response to paired pulses stimulation from controls and 6-OHDA mice (H) and the summarized results showing unaltered pared-pulse ratios between groups. **J-L**) Representative traces of optogenetically-evoked thalamic EPSCs recorded at -80 mV and +40 mV in PT neurons from controls and 6-OHDA mice. Dashed lines indicate where AMPARs- and NMDARs-mediated responses were measured to quantify NMDA/APMA ratio (K) and AMPARs rectification (L). Summarized results showing no change in the NMDA/AMPA ratio (K) and AMPARs rectification index (L) between groups.

Thalamic axon terminals target the dendritic spines and dendritic shaft of M1 PT neurons (Hooks et al., 2013; Kuramoto et al., 2009; Villalba et al., 2021). To interrogate postsynaptic structural changes associated with DA degeneration, the density of dendritic spines and the diameter of dendritic shaft of M1 PT neurons were assessed in slices from controls and 6-OHDA mice that received AAVrg-hSyn-eGFP injections into the pontine nuclei (**Figure 3D, E**). The density of spines on the basal dendrites in the layer V from 6-OHDA mice decreased significantly relative to those from controls (spine density of basal dendrites, control = 6.4 [5.4–7.1] per 10 μm, n = 53 segments/3 mice; 6-OHDA = 4.7 [3.6–5.5] per 10 μm, n = 47 segments/3 mice; $p < 0.001$, MWU; **Figure 3D-F**). Similarly, the densities of eGFP-labeled spines on the L1 apical dendrites also decreased significantly in slices from 6-OHDA mice relative to those from controls (spine density of L1 apical dendrites, controls = 2.6 [2.3–3.2] per 10 μm, n = 24 segments/3 mice; 6-OHDA = 1.7 [1.3–3.1] per 10 μm, n = 25 segments/3 mice; p = 0.02, MWU, **Figure 3F**). Further, the diameters of both L5 basal dendrites (control = 0.9

216 [0.77–1.06] μm, n = 262 samples/3 mice; 6-OHDA = 0.57 [0.44–0.67], n = 267
217 samples/3 mice; $p < 0.0001$, MWU; **Figure 3G**) and L1 apical dendrites (control = 0.59
218 [0.5–0.74] μm, n = 240 samples/3 mice; 6-OHDA = 0.46 [0.42–0.57], n = 240 samples/3
219 mice; $p < 0.0001$; MWU; **Figure 3G**) were decreased significantly in slices from 6-
220 OHDA mice relative to those from controls. The above data suggest that SNc DA
221 degeneration induces loss of dendritic spines and shrunk dendritic shafts of M1 PT
222 neurons. Combining structural changes at both the pre- and post-synaptic sides (**Figure**
223 **3A-G**), we conclude that degeneration of SNc DA neurons induces a loss of
224 thalamocortical synapses to M1 PT neurons.
225
226 **SNc DA degeneration does not alter postsynaptic receptor properties of**
227 **thalamocortical synapses to M1 PT neurons**
228 Next, we assessed function adaptations at thalamocortical inputs to M1 PT neurons
229 following the loss of SNc DA neurons. There was no significant change in the paired
230 pulse ratio (PPR) of thalamocortical oEPSCs in PT neurons from control and 6-OHDA
231 mice (control = 0.49 [0.39–0.66], n= 62 neurons/7 mice; 6-OHDA = 0.52 [0.38–0.75], n =
232 73 neurons/8 mice; $p = 0.1$, MWU; **Figure 3H, I**). It suggests that the decreased
233 thalamocortical projection to PT neurons was not due to a lower initial release
234 probability at thalamic axon terminals.
235 To assess postsynaptic adaptations at thalamocortical synapses to PT neurons,
236 we measured the ratio of EPSCs mediated by NMDA receptors (Rs) and AMPARs
237 (NMDA/AMPA ratio) as well as AMPARs rectification properties between controls and 6-
238 OHDA mice. There was no difference in the NMDA/AMPA ratio at thalamic projections

239 to PT neurons between groups (control = 0.62 [0.44–0.91], n = 34 neurons/4 mice; 6-
240 OHDA = 0.63 [0.29–1.0], n = 38 neurons/5 mice; *p* = 0.85, MWU; **Figure 3J, K**).
241 Moreover, there was no alteration in the inward rectification index of AMPARs at
242 thalamic projections to PT neurons (control = 0.47 [0.37–0.6], n = 34 neurons/4 mice; 6-
243 OHDA = 0.52 [0.39–0.94], n = 38 neurons/5 mice; *p* = 0.22, MWU; **Figure 3J, L**). These
244 data suggest that SNc DA degeneration does not alter the relative contributions of
245 postsynaptic AMPARs- and NMDARs-mediated transmission or change the subunit
246 composition of AMPARs at thalamic projections to M1 PT neurons.

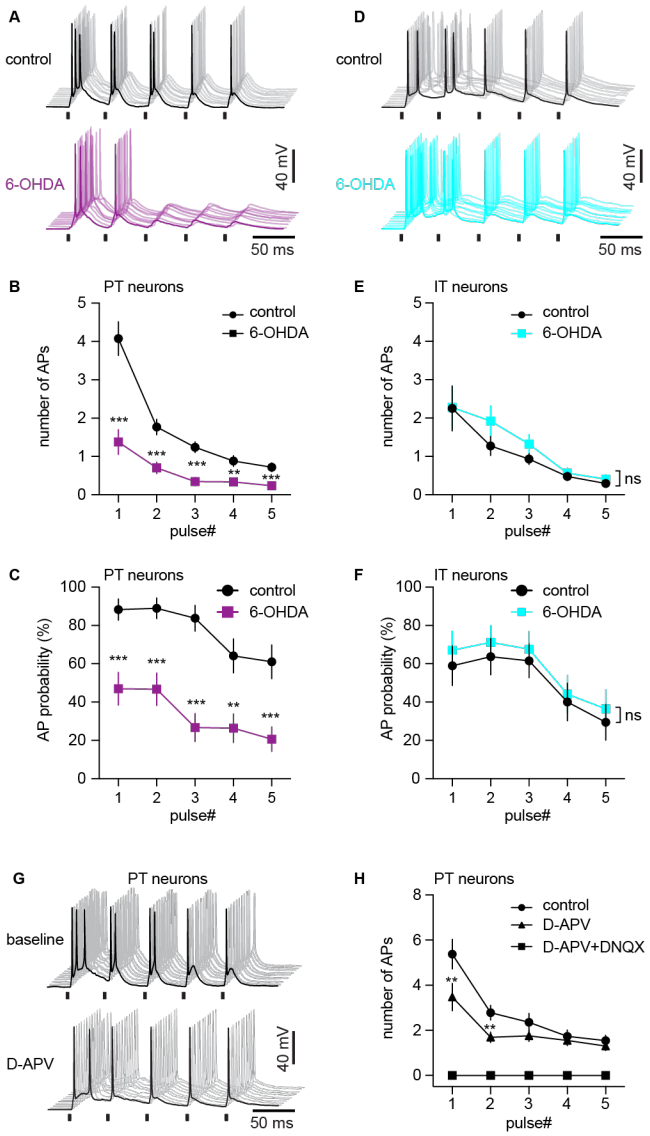

247

248

Figure 4. SNc DA degeneration decreases the effectiveness of thalamic driving of M1 PT neuronal firing. **A**) Representative traces of AP firing of M1 PT neurons from controls and 6-OHDA mice in response to 20 Hz optogenetic stimulation. AP traces from 10 trials were aligned for both groups. **B-C**) Summarized results show that both the number (B) and probability (C) of synaptically-generated APs in M1 PT neurons decreased significantly in 6-OHDA mice relative to controls. **D**) Representative traces of AP firing of M1 IT neurons from controls and 6-OHDA mice in response to 20 Hz optogenetic stimulation. **E-F**) Summarized results show that the number (E) and probability (F) of synaptically-generated APs in M1 IT neurons was not altered in 6-OHDA mice relative to controls. **G**) Representative traces of AP firing of M1 PT neurons in response to 20 Hz optogenetic stimulation prior to and after D-APV application. **H**) Summarized results show that NMDARs blockade using D-APV decreased the number of APs of PT neurons generated by thalamic stimulation.

249

250 **SNc DA degeneration decreases the effectiveness of thalamic driving of M1 PT**

251 **neuronal firing**

252 Loss of SNc DA neurons selectively decreases the intrinsic excitability of M1 PT

253 neurons (Chen et al., 2021). Together with the decreased thalamocortical synaptic

254 strength of PT neurons, a corollary prediction would be a reduced effectiveness of

255 thalamic driving of M1 PT neuronal firing following the loss of SNc DA neurons. To test

256 this hypothesis, we recorded retrogradely labelled PT and IT neurons under current

257 clamp mode and compared the effectiveness of thalamic excitation in driving the action

258 potential (AP) firing in controls and 6-OHDA mice (**Figure 4A, D**). A 20-Hz optogenetic

259 stimulation (1 ms duration) was delivered to activate ChR2-tagged thalamic axons in

260 M1, mimicking the synchronized β band bursting pattern of thalamocortical activity

261 observed in parkinsonian state (Brazhnik et al., 2016; Oswal et al., 2013). As predicted,

262 the effectiveness of thalamic driving of PT neuronal firing decreased significantly in

263 slices from 6-OHDA mice relative to those from controls (**Figure 4A-C**), as reflected by

264 a decreased number of APs per stimulation ($p < 0.0001$ for group difference, two-way

265 ANOVA followed by Sidak's tests; control = 29 neurons/3 mice; 6-OHDA = 33 neurons/4
266 mice; **Figure 4A, B**) and a decreased AP firing probability ($p < 0.0001$ for group
267 difference, two-way ANOVA followed by Sidak's tests; control = 29 neurons/3 mice; 6-
268 OHDA = 33 neurons/4 mice; **Figure 4A, C**). In contrast, we did not detect alterations in
269 the effectiveness of thalamic driving of IT neurons firing between groups ($p = 0.56$ for
270 group difference on AP probability; $p = 0.36$ for group difference on the number of APs;
271 control = 19 neurons/3 mice; 6-OHDA = 17 neurons/3 mice; two-way ANOVA, **Figure**
272 **4D-F**). Thus, these data suggest that loss of DA selectively disrupts the effectiveness of
273 thalamic excitation to drive PT neurons firing in M1.

274 To determine the relative contributions of AMPARs- and NMDARs-mediated
275 responses to thalamic driving of PT neurons firings, pharmacological approach was
276 used to assess the impact of NMDARs and AMPARs blockades on the number of
277 synaptically generated APs from PT neurons in control mice. The number of APs
278 generated by PT neurons in response to optogenetic stimulation of thalamic axon
279 terminals was significantly reduced by blockade of NMDARs using D-APV (50 μM),
280 particularly the number of APs generated by the first two stimulations (two-way ANOVA
281 followed by Sidak's tests; 13 neurons/3 mice **Figure 4G**). Synaptically generated APs of
282 PT neurons were abolished by the subsequent blockade of both NMDARs and AMPARs
283 using a mixture of D-APV (50 μM) and DNQX (20 μM) (**Figure 4H**). These data suggest
284 that both the NMDARs and AMPARs mediate thalamic driving of M1 PT neuron firing in
285 control mice. Altogether, the above results suggest that SNc DA degeneration
286 selectively decreases thalamocortical connectivity to M1 PT neurons and impairs the
287 effectiveness of thalamic driving of PT neuronal firing.

288 **Distinct properties of postsynaptic receptors at thalamic and sensory cortical**
289 **inputs to M1 PT neurons**

290 NMDA receptors play a critical role in thalamocortical synaptic integration and plasticity
291 during learning motor skills and contribute to adaptative changes in neurological
292 disorders (Guo et al., 2015b; Lafourcade et al., 2022; Miller et al., 2017). Next, we
293 tested the hypothesis that NMDARs at thalamocortical synapses mediate the selective
294 downregulation of thalamic excitation of PT neurons following the loss of SNc DA
295 neurons. To do this, we first measured the NMDA/AMPA ratio at thalamic projections to
296 PT and IT neurons (i.e., VM-PT and VM-IT synapses, respectively) as well as sensory
297 cortical synapses to PT neurons (i.e., SC-PT synapse) in controls. Interestingly, we
298 found a significantly higher NMDA/AMPA ratio at the thalamic synapses to PT neurons,
299 relative to thalamic projection to IT neurons or SC-PT synapses (NMDA/AMPA ratio,
300 VM-PT synapses = 0.62 [0.44–0.91], n = 34 neurons/4 mice; VM-IT synapse = 0.22
301 [0.16–0.33], n = 25 neurons/3 mice; SC-PT synapses = 0.34 [0.22–0.55], n = 19
302 neurons/3 mice; $p < 0.0001$; Kruskal-Wallis test followed by Dunn's test, **Figure 5A, B**).
303 These data suggest that NMDARs are functionally enriched at VM-PT synapses relative
304 to SC-PT or VM-IT synapses. In addition, there was a stronger inward rectification of
305 AMPARs at SC-PT synapses relative to thalamic projections to PT or IT neurons
306 (AMPARs rectification index, VM-PT synapses = 0.47 [0.37–0.60], n = 34 neurons/4
307 mice; VM-IT synapse = 0.91 [0.54–1.4], n = 25 neurons/3 mice; SC-PT synapses = 1.23
308 [0.97–2.32], n = 19 neurons/3 mice; $p < 0.0001$; Kruskal-Wallis test followed by Dunn's
309 test; **Figure 5A, C**). These data suggest GluA2-lacking, Ca^{2+}-permeable AMPARs are

enriched at SC-PT synapses relative to those from the motor thalamus to M1 PT or IT neurons in control mice.

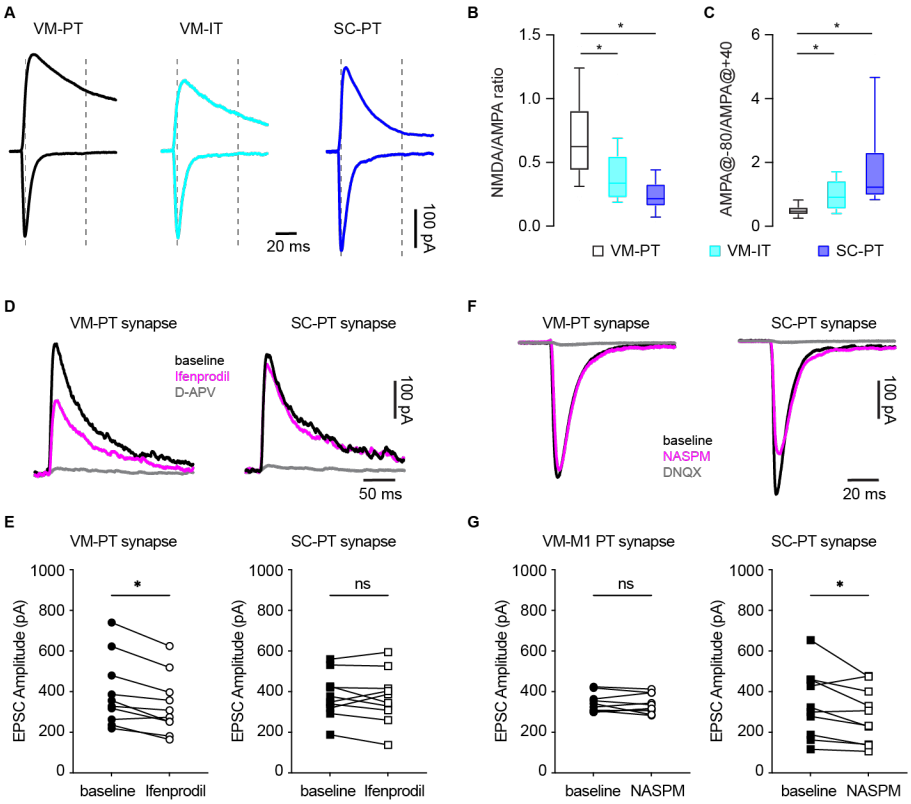

Figure 5. Distinct postsynaptic receptor properties at thalamic and sensory cortical inputs to PT neurons. **A**) Representative traces of AMPARs- and NMDARs-mediated responses from different synapses in M1. **B-C**) Box plots showing difference in the NMDA/AMPA ratios (**B**) and AMPARs rectification properties (**C**) of different synapses in M1. **D-E**) Pharmacology studies showing different sensitivities of NMDARs-mediated transmission at thalamic and sensory cortical synapses to ifenprodil. **D**) Representative traces of isolated NMDARs-mediated EPSCs from VM-PT and SC-PT synapses at baseline, in ifenprodil, and in ifenprodil plus D-APV. **E**) Box plots showing the effects of ifenprodil to the amplitude of NMDARs-mediated EPSCs at VM-PT (left) and SC-PT (right) synapses. **F**) Representative traces of AMPARs-mediated EPSCs from VM-PT and SC-PT synapses at baseline, in NASPM, and in NASPM plus DNQX. **G**) Box plots showing the effects of NASPM to the amplitude of AMPARs-mediated EPSCs at VM-PT (left) and SC-PT (right) synapses.

Next, pharmacological approaches were used to further confirm the synapse-specific properties of different inputs to M1 PT neurons in control mice. A large body of evidence suggests that GluN2B subunit-containing NMDA receptors with larger Ca^{2+}

317 conductance enriched at thalamocortical synapses in the prefrontal cortex and play a
318 critical role in pathological processes in neurological diseases (Miller et al., 2017; Wang
319 et al., 2008). Consistently, a noncompetitive antagonist of GluN2B-containing NMDARs
320 ifenprodil (3 μM) significantly and consistently reduced the amplitude of NMDARs-
321 EPSCs at VM-PT synapses (baseline = 342 [256–516] pA, ifenprodil = 292 [234–428]
322 pA; n = 10 neurons/4 mice; *p* = 0.004, WSR; **Figure 5D, E**), but not did not produce
323 consistent effect to the NMDA-EPSCs amplitude of SC-PT synapses (baseline = 363
324 [313–452] pA, ifenprodil = 366 [296–443] pA; n = 10 neurons/3 mice; *p* = 0.6, WSR;
325 **Figure 5D, E**). In addition, to quantitively assess the functional contribution of GluA2-
326 lacking, Ca^{2+}-permeable AMPARs at different inputs, a selective antagonist1-Naphthyl
327 acetyl spermine trihydrochloride (NASPM) was used. Bath application of NASPM (100
328 μM) consistently decreased the amplitude of AMPARs-EPSCs of SC-PT synapses
329 (baseline = 311 [181–459] pA; NASPM = 269 [106–419] pA; n = 10 neurons/ 4 mice; *p* =
330 0.02, WSR; **Figure 5F, G**), but did not produce significant effect to the amplitude of VM-
331 PT EPSCs (baseline = 333 [305–378] pA; NASPM = 327 [301–395] pA; n = 10 neurons/
332 4 mice; *p* = 0.6, WSR; **Figure 5F, G**).
333 Together, we conclude that GluN2B-containing NMDARs are enriched at
334 thalamic transmission to M1 PT neurons, and that GluA2-lacking, Ca^{2+}-permeable
335 AMPARs functionally contribute more to sensory cortical transmission to M1 PT
336 neurons under normal state.
337
338 **NMDARs mediate the decreased thalamocortical transmission to M1 PT neurons**

339 Prolonged activation of NMDARs by exogenously application of NMDA is sufficient to
340 mimic NMDAR-dependent synaptic and cellular plasticity in basal ganglia nuclei (Chu et
341 al., 2017; McIver et al., 2019). Given the enrichment of NMDARs at VM-PT synapses,
342 we further assessed if NMDARs activation mediates the decreased thalamocortical
343 synaptic strength to M1 PT neurons in parkinsonian state. Thus, brain slices from
344 controls and 6-OHDA mice were incubated with (1) normal ACSF, (2) NMDA-containing
345 ACSF (1 hour at 25 μM), or (3) D-APV/NMDA-containing ACSF for hours (Chu et al.,
346 2017), prior to physiological and anatomical studies (**Figure 6A**). In brain slices from
347 vehicle-injected control mice, NMDA incubation *ex vivo* reduced the amplitude of
348 thalamic oEPSCs of M1 PT neurons ($p < 0.0001$, two-way ANOVA followed by Sidak's
349 tests; **Figure 6B, D**), and the effects of NMDA could be abolished by D-APV and NMDA
350 co-incubation (**Supplementary Figure 1**). Interestingly, *ex vivo* NMDA incubation had
351 no effect on the amplitude of thalamic oEPSCs of M1 PT neurons from 6-OHDA mice
352 ($p > 0.79$; **Figure 6C, E**). These data suggest that chronic NMDARs activation is
353 sufficient to decrease the thalamic excitation to M1 PT neurons from control mice, but
354 such effects are occluded by 6-OHDA-induecd DA degeneration *in vivo*.
355 Since the degeneration of SNc DA neurons decreases the number of functional
356 thalamic inputs to M1 PT neurons (**Figures 2 & 3**), we further studied the impact of
357 exogenous NMDA incubation on Sr^{2+}-induced quantal glutamate release at
358 thalamocortical synapses to PT neurons. In slices from vehicle-injected controls, NMDA
359 incubation significantly decreased the frequency, but not the amplitude of
360 optogenetically evoked thalamic Sr^{2+}-EPSCs (frequency of Sr^{2+}-EPSCs in vehicle-
361 injected mice, control = 33.6 [21.1–50.4] Hz, n = 24 neurons/3 mice; NMDA = 10.9 [9.6–

362 12.9] pA; n = 24 neurons/3 mice; p = 0.001, MWU; amplitude of Sr^{2+}-EPSCs in vehicle-
363 injected mice, control = 12.5 [10.5–14.2] pA, n = 24 neurons/3 mice; NMDA = 19.4
364 [11.8–29.2] Hz, n = 24 neurons/3 mice; p = 0.1, MWU; **Figure 6F, G**). In contrast, in
365 slices from 6-OHDA mice, NMDA incubation did not alter the frequency or the amplitude
366 of optogenetically-evoked thalamic Sr^{2+}-EPSCs of PT neurons (frequency of Sr^{2+}-
367 EPSCs in 6-OHDA mice, control = 24.8 [15–37.4] Hz, n = 17 neurons/3 mice; NMDA =
368 25.6 [12.2–33.4] pA, n = 17 neurons/3 mice; p = 0.6, MWU; amplitude of Sr^{2+}-EPSCs in
369 6-OHDA mice; control = 12.9 [11.3–14.0] pA, n = 17 neurons/3 mice; NMDA = 11.2
370 [10.3–13.8] Hz, n = 27 neurons/3 mice; p = 0.21, MWU; **Figure 6H, I**). The above data
371 suggest that NMDARs activation reduces the number of functional thalamocortical
372 inputs to M1 PT neurons, but this effect was occluded in 6-OHDA mice.
373 Next, we studied whether *ex vivo* NMDA incubation could induce structural
374 changes at thalamocortical synapses to PT neurons. A separate set of brain slices from
375 controls and 6-OHDA mice were incubated with ACSF or NMDA-containing ACSF for 2
376 hours and then fixed with 4% PFA for immunohistochemistry studies. We found that *ex*
377 *vivo* NMDA incubation robustly decreased M1 L5 vGluT2 densities from slices of
378 controls, relative to those incubated in ACSF (vGluT2 densities from controls, ACSF =
379 12 [10–14.8] million/mm^3, n = 20 samples/3 mice; NMDA = 9 [7–10.8] million/mm^3, n =
380 16 samples/3 mice; p = 0.0016, MWU; **Figure 6J, K**). However, NMDA incubation did
381 not alter M1 L5 vGluT2 densities in slices from 6-OHDA mice (vGluT2 densities from 6-
382 OHDA mice, ACSF = 11 [8–12] million/mm^3, 20 samples/3 mice; NMDA = 11 [9–12]
383 million/mm^3, 20 samples/3 mice; p = 0.7, MWU; **Figure 6L, M**). In addition, NMDA
384 incubation also decreased the spine densities of L5 basal dendrites of retrogradely

385 labeled PT neurons from controls (spine density from controls, ACSF = 6 [5.4–7.6]
386 spines/10 μm, n = 24 samples/3 mice; and NMDA = 4.1 [3.5–4.9] spines/10 μm, n = 25
387 samples/3 mice; $p < 0.0001$, MWU; Figure N, O); but NMDA incubation did not alter
388 spine densities of PT neurons in slices from 6-OHDA mice (spine density from 6-OHDA
389 mice, ACSF = 4.3 [3.2–5] spines/10 μm, n = 29 samples/3 mice; NMDA = 3.7 [2.8–4.9]
390 spines/10 μm, n = 31 samples/3 mice; $p = 0.4$, MWU; **Figure 6P, Q**). Altogether, our
391 physiological and anatomical results suggest that excessive NMDARs activation is
392 sufficient to induce a reduced thalamocortical connection to M1 PT neurons, and that
393 DA degeneration likely recruits the NMDA-mediated mechanisms, leading to the
394 decreased thalamic excitation to M1 PT neurons in 6-OHDA mice.
395 Our recent work also showed that loss of DA decreases the intrinsic excitability of
396 M1 PT neurons (Chen et al., 2021). Whether the intrinsic and synaptic adaptations in
397 PT neurons share the same NMDA-mediated mechanisms remain unknown. To
398 address this question, we studied the impact of NMDA incubation on cellular excitability
399 of M1 PT neurons from control mice. Interestingly, exogenous NMDA incubation did not
400 alter the cellular excitability of PT neurons in slices from controls (**Supplementary**
401 **Figure 2**). The above data indicate chronic NMDARs activation was not sufficient or
402 necessary to trigger intrinsic adaptations in M1 PT neurons. Taken together, these data
403 suggest that (1) NMDARs activation *ex vivo* was sufficient to decrease thalamocortical
404 transmission in slice from control mice; (2) in DA depleted 6-OHDA mice NMDARs-
405 mediated reduction of thalamocortical transmission to PT neurons *in vivo* occluded the
406 effect of NMDAR activation *ex vivo*; and (3) distinct molecular mechanisms mediate the

407 intrinsic and synaptic adaptations in M1 PT neurons following the degeneration of SNc

408 DA neurons.

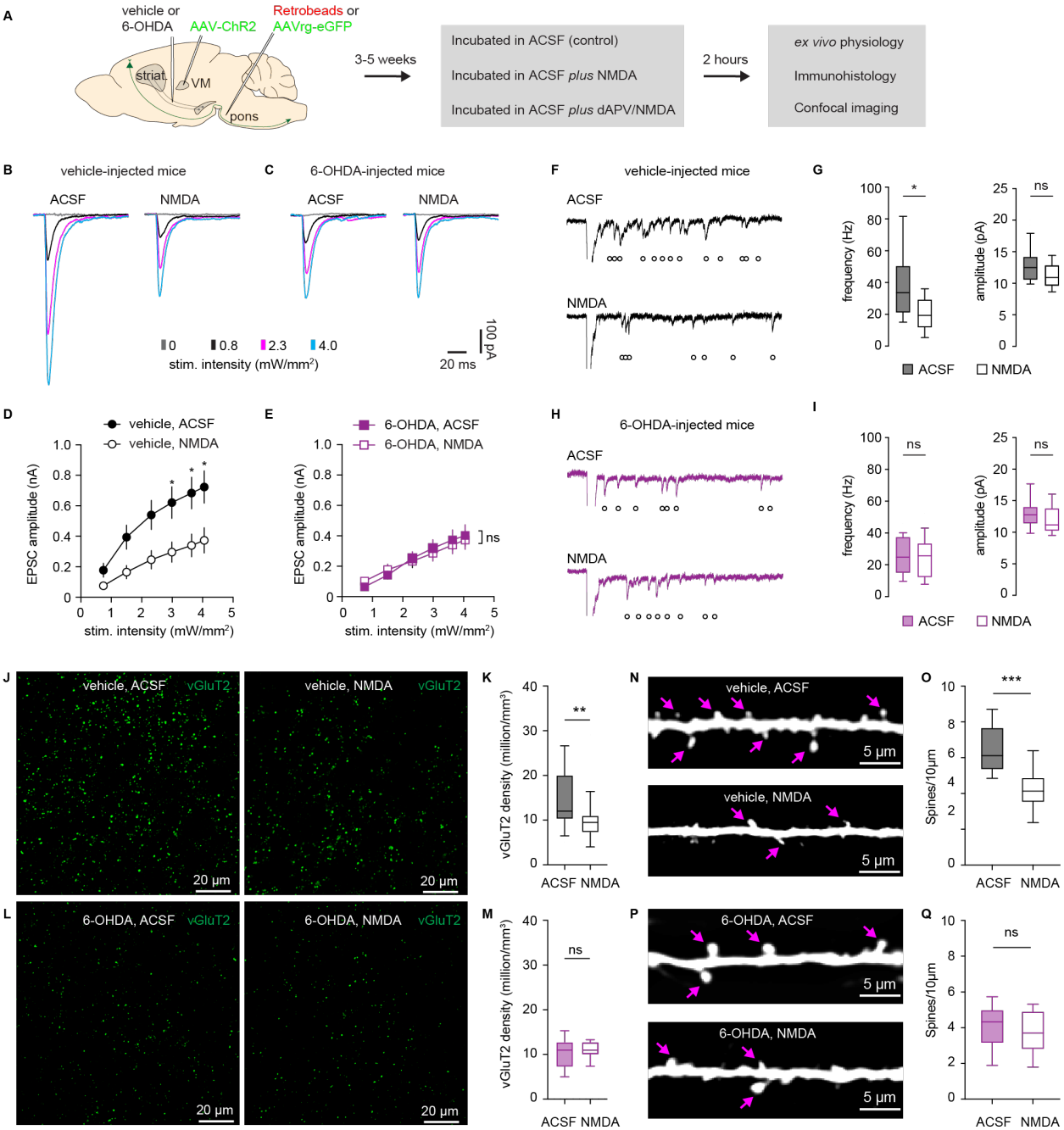

409

Figure 6. Excessive NMDARs activation mediates the impaired thalamocortical transmission following SNc DA degeneration. **A**) Experimental design. **B-C**) Representative traces of optogenetically-evoked thalamocortical EPSCs of PT neurons from vehicle-injected controls (B) and 6-OHDA-injected mice (C), which were either incubated in normal ACSF (control) or ACSF containing NMDA (25 μM). **D-E**) Summarized results show that NMDA incubation decreased the amplitude of oEPSCs from slices of vehicle-injected controls (D), but not those from slices of 6-OHDA-injected mice (E). **F-G**) NMDA incubation decreased the frequency but not the amplitude of optogenetically-evoked Sr^{2+}-EPSCs in slice from vehicle-injected controls. **F**) Representative traces of Sr^{2+}-EPSCs. **G**) Summarized results. **H-I**) NMDA incubation did not alter the frequency and the amplitude of optogenetically-evoked Sr^{2+}-EPSCs in slice from 6-OHDA-injected mice. **H**) Representative traces of Sr^{2+}-EPSCs. **I**) Summarized results. **J**) Representative confocal images of vGluT2 immunoreactivity from ACSF- and NMDA-treated slices of controls. **K**) Box plot shows that NMDA incubation reduced vGluT2 densities in slices of controls. **L**) Representative confocal images of vGluT2 immunoreactivity from ACSF- and NMDA-treated slices of 6-OHDA. **M**) Box plot shows that NMDA incubation did not affect vGluT2 densities in slices of 6-OHDA mice. **N**) Representative confocal images of M1 L5 dendritic spines from ACSF- and NMDA-treated slices of controls. **O**) Box plot shows that NMDA incubation reduced L5 spine densities in slices of controls. **P**) Representative confocal images of M1 L5 dendritic spines from ACSF- and NMDA-treated slices of 6-OHDA mice. **Q**) Box plot shows that NMDA incubation did not alter L5 spine densities in slices from 6-OHDA mice. Arrows in (N and P) indicate representative spines on dendrites.

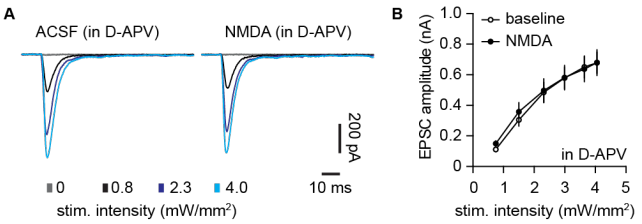

Supplementary Figure 1. NMDA-induced reduction of thalamocortical transmission was blocked by D-APV. **A**) Representative traces of optogenetically-evoked thalamocortical EPSCs from PT neurons. **B**) Summarized data.

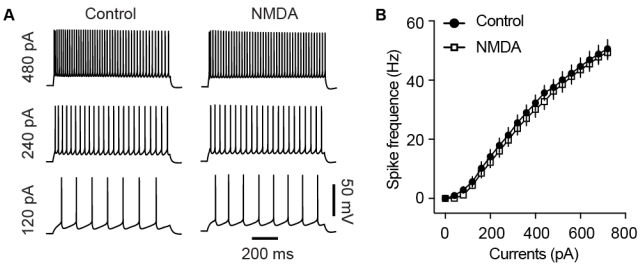

Supplementary Figure 2. *Ex vivo* NMDA receptor activation does not affect cellular excitability of M1 PT neurons. **A**) Representative traces of action potentials of PT neurons from slices treated with normal ACSF (control) or ACSF containing NMDA (25 μM). **B**) Summarized data.

414

415 **Basal ganglia outputs drive the decreased thalamocortical transmission following**

416 **the degeneration of SNc DA neurons**

417 Cortico-basal ganglia network shows an exaggerated oscillatory and bursting pattern of

418 activity following the loss of SNc DA neurons (Galvan and Wichmann, 2008; Oswal et

419 al., 2013). We posited that the rhythmic and bursting outputs of the basal ganglia

420 promote NMDARs activation at the thalamocortical synapses to M1 PT neurons, and

421 that prolonged NMDARs activation further contributes to the decreased thalamocortical

422 excitation to PT neurons. Thus, we employed chemogenetic approaches to suppress

423 basal ganglia output *in vivo* and studied whether M1 circuitry dysfunction in 6-OHDA

424 mice could be rescued by inhibiting pathologic basal ganglia outputs.

425 PV-Cre knockin mice were unilaterally injected with vehicle or 6-OHDA into the

426 MFB, plus AAV9-hSyn-FLEX-hM4Di-mCherry into the SNr of the same hemisphere for

427 chemogenetic manipulation of basal ganglia outputs (**Figure 7A**). Immunofluorescence

428 staining showed a selective expression of hM4Di (Gi)-DREADDS on SNr PV-expressing

429 cells (**Figure 7A**). There was no difference in the number of hM4Di-expressing cells in

430 the SNr between 6-OHDA mice and controls (controls = 276 [160–357] neurons/slice, n

431 = 20 slices/10 mice; 6-OHDA = 233 [170–271] neurons/slice, n = 23 slices/12 mice; p =

432 0.08, MWU). Loose-sealed cell-attached recordings showed that bath application of

433 DREADDS agonist CNO (10 μM) effectively suppressed the frequency and regularity of

434 autonomous firing of SNR neurons from 6-OHDA mice (frequency, baseline = 5.2 [4.3–

435 7.5] Hz, CNO = 3.9 [0.27–5.6] Hz; n = 10 neurons/3 mice; p = 0.02, WSR; **Figure 7C**;

436 CV of ISIs, baseline = 0.27 [0.13–0.49], CNO = 0.61 [0.19–1.35]; n = 10 neurons/3

437 mice; p = 0.016, WSR; **Figure 7D**).

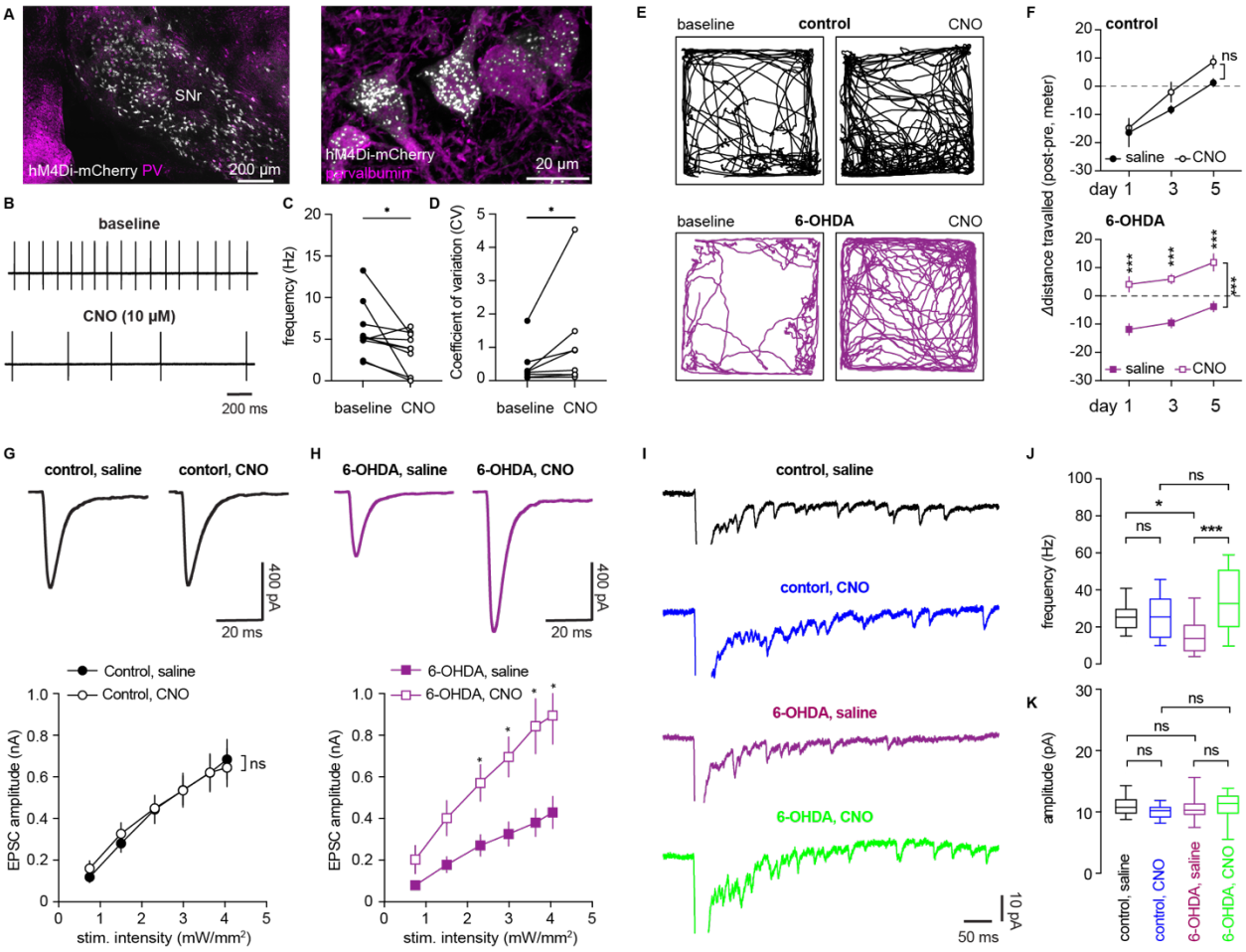

438

Figure 7. Basal ganglia output drives the synaptic adaptations in M1 following the loss of SNc DA neurons. **A**) Representative confocal images showing hM4Di-mcherry expression in the PV-expressing SNr neurons under low and high magnifications. **B**) Representative traces of the autonomous firing of SNr neurons from a 6-OHDA mice prior to and after CNO application. **C-D**) Box plots showing that hM4Di activation by CNO effectively suppressed the frequency (C) and regularity (D) of SNr neurons firing. **E**) Representative track plots showing the effects of CNO injections to locomotor activity of controls and 6-OHDA mice in an open field on day 5. **F**) Summarized results showing the difference of distance travelled in the open field between pre- and post-saline/CNO injections in controls and 6-OHDA mice. Behavioral tested were conducted on days 1, 3 and 5. **G-H**) hM4Di activation by CNO injection did not alter the amplitude of optogenetically thalamocortical EPSCs in PT neurons from controls (G), but it induced an increased optogenetically thalamocortical EPSCs in PT neurons from 6-OHDA mice (H). Top, representative traces of oEPSCs in PT neurons; Bottom, summarized results. **I**) Representative traces of optogenetically-evoked Sr^{2+}-EPSCs in controls and 6-OHDA mice treated with saline or CNO. **J**) Summarized results showing CNO injection did not alter the frequency of Sr^{2+}-EPSCs in slices from controls, but decreased the frequency of Sr^{2+}-EPSCs in slices from 6-OHDA mice. **K**) Summarized results showing CNO injection did not alter the amplitude of Sr^{2+}-EPSCs in slices from either controls or 6-OHDA mice.

PV-Cre mice with SNr hM4Di expression were injected with either CNO (1.0 mg/kg, S.C., at ~12 hrs interval between injections) or saline for 5 consecutive days to continuously suppress abnormal basal ganglia outputs, or control for subcutaneous injections. Open filed locomotor activities were measured on days 1, 3 and 5. CNO injection tended to increase the distance travelled of control mice in an open field (**Figure 7E**), but such effects were not distinguishable from saline-injected control mice (**Figure 7F**). This is perhaps because that CNO's effects to neuronal activity of the unilateral SNr of DA intact mice were not sufficient to robustly affect general motor activity. In contrast, CNO injection significantly increased the locomotor activity of 6-OHDA mice relative to saline injected mice (**Figure 7E, F**). These data indicate that the SNr neurons of 6-OHDA mice were more sensitive to hM4Di activation and that chemogenetic suppression of SNr output of 6-OHDA mice was associated with immediate behavioral effects. These results also confirm that chemogenetic approach

453 could effectively suppress basal ganglia outputs and led to physiological and behavioral
454 phenotypes.
455 To determine whether suppression of basal ganglia outputs could rescue
456 adaptive changes of M1 circuits, the same cohort of mice described above also
457 received retrobeads injection into the pons to retrogradely label M1 PT neurons and
458 ChR2(H134R)-eYFP injection into the motor thalamus for optogenetic stimulation of
459 thalamocortical synapses to PT neurons. In vehicle-injected control mice, we found that
460 chemogenetic suppression of SNr activity through repetitive CNO injection did not alter
461 the amplitude of optogenetically evoked thalamic oEPSCs in PT neuros (p = 0.9, two-
462 way ANOVA; **Figure 7G**). In contrast, repetitive CNO injection significantly increased
463 the amplitude of optogenetically evoked thalamic oEPSCs in PT neurons of 6-OHDA
464 mice (p = 0.007, two-way ANOVA followed by Sidak's; **Figure 7H**).
465 Further, we assessed the effects of chemogenetic suppression of SNr activity to
466 quantal properties of thalamocortical transmission to M1 PT neurons by replacing
467 extracellular Ca^{2+} with Sr^{2+}. Chemogenetic suppression of SNr activity through repetitive
468 CNO injection did not alter either the frequency or the amplitude of optogenetically-
469 evoked thalamic Sr^{2+}-EPSCs in PT neuros of vehicle-injected control mice (frequency of
470 Sr^{2+}-EPSCs, control/saline = 25 [19–30] Hz, control/CNO = 25 [14–35] Hz; $p > 0.9$;
471 amplitude of Sr^{2+}-EPSCs, control/saline = 10.7 [9.7–12.1] pA, n= 18 neurons/3 mice;
472 control/CNO = 10.2 [9.1–10.9] pA, n = 18 neurons/3 mice; p = 0.8, Kruskal-Wallis test
473 followed by Dunn's tests, **Figure 7I-K**). In contrast, repetitive CNO injection significantly
474 increased the frequency, but not the amplitude, of optogenetically evoked thalamic Sr^{2+}-
475 EPSCs in PT neurons of 6-OHDA mice (frequency of Sr^{2+}-EPSCs, 6-OHDA/saline =

476 13.8 [6.7–21.3] Hz, 6-OHDA/CNO = 32.4 [19.6–50.8] Hz, p = 0.0001; amplitude of Sr^{2+}-
477 EPSCs, 6-OHDA/saline = 10.3 [9.5–11.4] pA, n= 22 neurons/3 mice; 6-OHDA/CNO =
478 11.4 [9.7–12.7] pA, n = 19 neurons/3 mice; p = 0.95, Kruskal-Wallis test followed by
479 Dunn's tests, **Figure 7I-K**). Together, these data suggest that chemogenetic
480 suppression of basal ganglia outputs could rescue the decreased thalamocortical
481 transmission to M1 PT neurons in 6-OHDA mice.

482 Our recent study reported a decreased intrinsic excitability of M1 PT neurons in
483 parkinsonism (Chen et al., 2021). To interrogate the impact of chemogenetic
484 suppression of basal ganglia output on cellular excitability of M1 PT neurons,
485 retrogradely labelled PT neurons were targeted for current clamp recording. In vehicle-
486 injected control mice, continuous CNO injections for 5 days did not alter the intrinsic
487 excitability of M1 PT neurons (p = 0.29, two-way ANOVA, **Supplementary Figure 3**). In
488 6-OHDA mice, CNO injections for 5 days tended to increase the excitability of M1 PT
489 neurons, but the effects did not reach statistical significance (p = 0.18, two-way ANOVA,
490 **Supplementary Figure 3**). These data suggesting that adaptation of the intrinsic
491 excitability of PT neurons perhaps involves additional mechanisms.

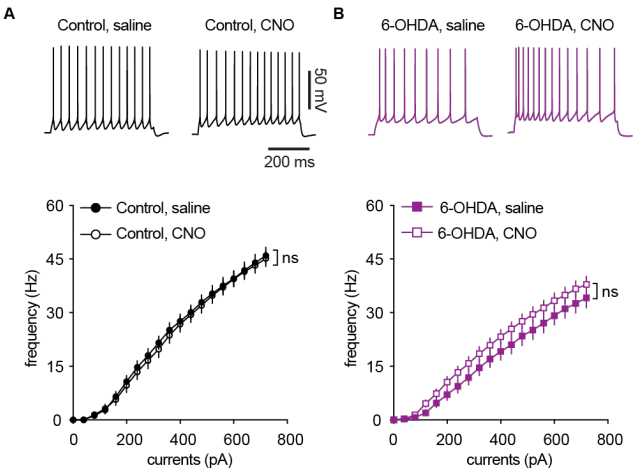

492

Supplementary Figure 3. Chemogenetic suppression of basal ganglia output does not affect intrinsic excitability of M1 PT neurons. **A**) Representative traces of action potentials of PT neurons from saline- and CNO-injected control mice (top) and summarized results (bottom). **B**) Representative traces of action potentials of PT neurons from saline- and CNO-injected 6-OHDA mice (top) and summarized results (bottom).

496 **Discussion**

497 The present study provides novel insights into motor cortical circuitry adaptations
498 following the degeneration of SNc DA neurons in parkinsonism. We demonstrated that
499 degeneration of SNc DA neurons induces cell-subtype- and input-specific
500 downregulation of thalamic excitation to M1 PT neurons (**Figure 1**). Our physiological
501 and anatomical analyses showed that the weakened thalamocortical synaptic strength
502 is likely caused by a loss of thalamocortical synapses (**Figure 2–4**). We further found
503 that NMDARs are enriched at thalamocortical synapses to M1 PT neurons (**Figure 5**).
504 Prolonged NMDARs activation *ex vivo* was sufficient to decrease thalamocortical
505 excitation to M1 PT neurons from control animals, but such effects could be abolished
506 by D-APV pretreatment and were occluded in slices from 6-OHDA mice (**Figure 6**).
507 These data suggest that excessive NMDARs activation *in vivo* is involved in mediating
508 the decreased thalamocortical connection strength following the degeneration of SNc
509 DA neurons. In addition, we showed that chemogenetic suppression of the SNr activity
510 can reverse the disrupted thalamocortical transmission in 6-OHDA mice (**Figure 7**),
511 suggesting that pathological activity of basal ganglia perhaps drives cortical circuitry
512 dysfunction following the degeneration of SNc DA neurons. Last, we showed that
513 synaptic and intrinsic adaptations of M1 PT neutrons in parkinsonism do not share the
514 common NMDARs-mediated molecular mechanisms.

515

516 *Motor cortical circuits dysfunction in parkinsonism*

517 It has been long thought that the hypoactivity of the motor cortex in PD is due to direct
518 and acute effects of an elevated basal ganglia inhibition following the degeneration of

519 SNc DA neurons. However, this model can't explain the cell-subtype-specific decrease
520 of PT (but not IT) neuronal activity in DA-depleted animals (Pasquereau and Turner,
521 2011), particularly considering that PT and IT neurons in M1 receive similar levels of
522 thalamic excitation (Hooks et al., 2013). In addition, M1 circuits faces several
523 perturbations in parkinsonism, e.g., decreased dopaminergic/noradrenergic
524 neuromodulation (Gaspar et al., 1991; Vitrac and Benoit-Marand, 2017) and
525 elevated/pathologic basal ganglia outputs. Thus, it is plausible that such circuitry
526 perturbations engage homeostatic plasticity mechanisms to stabilize the neuronal and
527 circuit activity (Turrigiano, 2011). As expected, we observed a series of intrinsic (Chen
528 et al., 2021) and synaptic adaptations in M1 following the degeneration of SNc DA
529 neurons (**Figures 1–4**), which mainly occur in PT neurons. Thalamocortical
530 transmission and plasticity play critical roles in the acquisition (Biane et al., 2016) and
531 execution (Sauerbrei et al., 2020) of skilled motor activity. Thus, the decreased
532 thalamocortical connection strength (**Figure 1**) could contribute to the reduced
533 magnitude and disputed temporal pattern of PT neuronal activation *in vivo* at the onset
534 of skilled movements in parkinsonian mice and NHP (Aeed et al., 2021; Hyland et al.,
535 2019; Pasquereau et al., 2016).
536 The reduced frequency of PT neurons firing can be caused by combined effects
537 of intrinsic and synaptic adaptations, but these adaptive changes still can't provide
538 meaningful explanation for the enhanced synchronized bursting pattern of activity of M1
539 PT neurons in parkinsonian animals (Goldberg et al., 2002; Pasquereau et al., 2016).
540 Future detailed circuitry analyses at cellular and synaptic levels using optogenetics-

541 assisted circuitry interrogations and computational approaches are needed to provide a
542 better understanding of motor cortical dysfunction in parkinsonism.
543
544 *Molecular and circuitry mechanisms underlying motor cortical dysfunction*
545 Our data show that NMDARs are enriched at thalamocortical synapses M1 PT neurons
546 (**Figure 5**). Such NMDARs enrichment can play critical role in the synaptic plasticity at
547 thalamocortical synapses during motor learning (Biane et al., 2016; Bruno and
548 Sakmann, 2006; Guo et al., 2015b; Xu et al., 2009). Based on these basic biophysical
549 properties, we predicted that excessive activation of NMDARs during the synchronized
550 bursting pattern of PT neuronal activity in parkinsonian state would mediate the
551 pathological loss of thalamocortical connection in 6-OHDA mice. Consistently we
552 showed that prolonged NMDARs activation is sufficient to decreased thalamocortical
553 connections in controls, but not in the 6-OHDA mice (**Figure 6**). Similar NMDARs-
554 mediated maladaptive changes have been reported in the subthalamic nucleus and the
555 medial prefrontal cortex in neurological disorders (Chu et al., 2017; Miller et al., 2017).
556 Therefore, compartment specific innervation of M1 PT neurons by the thalamic inputs
557 and the unique postsynaptic receptor compositions can be key molecular and synaptic
558 mechanisms mediating their selective downregulation in parkinsonian state (Lafourcade
559 et al., 2022).
560 Chronic suppression of basal ganglia outputs in 6-OHDA mice rescued the
561 decreased thalamocortical transmission, arguing that the excessive pathological signals
562 from the basal ganglia drive the adaptive changes in the M1. Consistently, recent
563 studies have reported that synchronized bursting pattern of basal ganglia outputs can

564 induce rebound firing of downstream targets, e.g., neurons in the motor thalamus and
565 superior colliculus, and trigger the associated motor activities (Kim et al., 2017;
566 Villalobos and Basso, 2022). Thus, we posit that the excessive basal ganglia outputs
567 synchronize motor thalamic neuronal activity *in vivo* (Brazhnik et al., 2016; Kim et al.,
568 2017), leading to a prolonged activation of NMDARs at thalamocortical synapses in M1
569 and a subsequent downregulation of their functional connection.
570
571 *Conclusion*
572 Altogether, we demonstrated that degeneration of SNc DA neurons in parkinsonism
573 triggers cell-subtype- and synapse-specific adaptations in M1, which can be important in
574 the pathophysiology of motor deficits in PD. Moreover, our studies also highlight that
575 synaptic and intrinsic alterations in M1 are mediated by different circuitry and molecular
576 mechanisms. While thalamocortical synaptic adaptations are likely caused by
577 excessively synchronized basal ganglia outputs and the associated NMDARs activation,
578 additional mechanisms seem to be involved into the intrinsic adaptations of M1 PT
579 neurons following the loss of DA neurons. Further studies remain needed for better
580 understanding of motor cortical dysfunction in parkinsonism.
581
582
583
584

585 **Materials and Methods**

586 *Animals*

587 Wild-type (WT) C57BL/6J mice of both sexes (3–4 month-old,
588 RRID:IMSR_JAX:000664) were obtained from the Van Andel Research Institute
589 vivarium internal colony and used in the study. Homozygous PV-Cre knock-in mice
590 were originally purchased from Jackson laboratories (stock# 017320RRID:
591 IMSR_JAX:017320, Bar Harbor, ME) and maintained at a C57/BL6J background in Van
592 Andel Research Institute vivarium. Mouse genotyping was conducted through the
593 service of Transnetyx, Inc (Cordova, TN). Mice were housed up to four animals per
594 cage under a 12/12 h light/dark cycle with access to food and water *ad libitum* in
595 accordance with NIH guidelines for care and use of animals. All animal studies were
596 reviewed and approved by the Institutional Animal Care and Use Committee at Van
597 Andel Research Institute (reference#: 22-02-006).

598

599 *Stereotaxic surgery for 6-OHDA and virus injections*

600 Mice were randomly assigned to different treatment groups. Mice were mounted and
601 secured in a stereotaxic frame (Kopf) under 2% isoflurane anesthesia. Throughout the
602 procedure, body temperature of the mouse was maintained by a thermostatic heating
603 pad. Once the skull was opened, small holes were drilled above the pre-determined
604 targets to inject: 1) 6-OHDA (3–4 μg) into the medial forebrain bundle (MFB, from
605 bregma (in mm), anterior-posterior (AP) = -0.7, mediolateral (ML) = +1.2, and
606 dorsoventral (DV) = -4.7 from the brain surface) to induce unilateral degeneration of
607 nigrostriatal pathway, or vehicle into the MFB to serve as vehicle-injected controls; 2)

608 retrobeads (200 nl, 10x dilution) into the ipsilateral pontine nuclei (from bregma (in mm),
609 AP = -5.0, ML = +0.6, DV = -5.0) or contralateral striatum (from bregma (in mm), AP =
610 +0.2, ML = -2.3, DV = -2.9) to retrogradely label PT and IT neurons, respectively; and 3)
611 AAV9-hSyn-ChR2(H134R)-eYFP (RRID:Addgene_127090, 300 nl at a titer of $3.6x10^{12}$
612 GC/ml) into the ventral medial region of the thalamus (from bregma (in mm), AP = -1.6,
613 ML = 0.8, DV = -4.3) to label thalamocortical axon terminals for optogenetics studies. A
614 small cohort of mice also received pAAV9-hSyn-DIO-hM4D(Gi)-mCherry
615 (RRID:Addgene_44362, 300 nl at a titer of $2.2x10^{12}$ GC/ml) injection into the substantia
616 nigra pars reticulata (from bregma (in mm), AP = -3.4, ML = +1.4, DV = -4.6) for
617 chemogenetic studies. For morphology studies, AAVrg-hSyn-eGFP
618 (RRID:Addgene_50465, 300 nl at 2x 10^{13} GC/ml) were injected into the pontine nuclei to
619 regrogradely label PT neuron in the motor cortex. All injection were performed using a
620 10 µl syringe (Hamilton, Reno, NV) mounted on a motorized microinjector (Stoelting,
621 Wood Dale, IL) at a speed of 100 nl/min. Details of the stereotaxic injections procedure
622 can be found on Protocol.io (dx.doi.org/10.17504/protocols.io.rm7vzye28lx1/v1)
623
624 *Slice preparation for electrophysiology*
625 3–4 weeks post-injections, brain slices were prepared for electrophysiology. Mice were
626 anesthetized with avertin (250–300 mg/kg), followed by transcardial perfusion with ice-
627 cold sucrose-based artificial cerebrospinal fluid (aCSF) equilibrated with 95% O_2/5%
628 CO_2 and containing (in mM): 230 sucrose, 26 $NaHCO_3$, 10 glucose, 10 MgSO4, 2.5 KCl,
629 1.25 NaH_2PO_4, 0.5 $CaCl_2$, 1 sodium pyruvate and 0.005 L-glutathione. Coronal brain
630 sections (250 µm) containing the primary motor cortex were prepared using a vibratome

631 (VT1200s, Leica, RRID:SCR_018453) in the same sucrose-based solution that was
632 maintained at ~4 °C using a recirculating chiller (FL300, Julabo, Allentown, PA). Slices
633 were then held in aCSF equilibrated with 95% O_2/5% CO_2 and containing (in mM): 126
634 NaCl, 26 $NaHCO_3$, 10 glucose, 2 $MgSO_4$, 2.5 KCl, 1.25 NaH_2PO_4, 1 sodium pyruvate
635 and 0.005 L-glutathione at 35 °C for 30 min for recovery and then at room temperature
636 until electrophysiology recordings or NMDA incubation.
637
638 *Brain slice physiological recordings and optogenetics*
639 Brain slices were placed in recording chamber with continuous perfusion of recording
640 solution containing (in mM): 126 NaCl, 26 $NaHCO_3$, 10 glucose, 3 KCl, 1.6 $CaCl_2$, 1.5
641 $MgSO_4$, and 1.25 NaH_2PO_4. The solution was equilibrated with 95% O_2/5%CO_2 and
642 maintained at 33–34 °C using feedback controlled in-line heater (TC-324C, Warner
643 Instruments). To assess synaptic strength, TTX (1 μM) and 4-AP (100 μM) were
644 routinely included to isolate optogenetically evoked monosynaptic thalamocortical or
645 corticocortical EPSCs in M1. To test the effectiveness of thalamic driving of M1
646 neuronal firing (Figure 4), TTX/4-AP were omitted from the recording solution and a
647 selective $GABA_A$ receptor antagonist SR-95531 (GABAzine) was added to prevent the
648 recruitment of GABAergic inhibitions. Neurons were visualized using a CCD camera
649 (SciCam Pro, Scientifica, UK) and SliceScope Pro 6000 system (Scientifica, UK)
650 integrated with a BX51 upright microscope and motorized micromanipulators.
651 Retrogradely labelled neurons in the layer 5 were targeted under a 60x water immersion
652 objective lens (Olympus, Japan) for whole-cell patch clamp recording using a
653 MultiClamp 700B amplifier (RRID:SCR_018455) and Digidata 1550B controlled by

654 pClamp 11 software (Molecular Devices, San Jose, CA; RRID:SCR_011323). Data
655 were sampled at 50 KHz. Borosilicate glass pipettes (O.D. = 1.5 mm, I.D. = 0.86 mm,
656 length = 10 cm, item#: BF150-86-10, Sutter Instruments, Novato, CA) were pulled by
657 micropipette puller (P1000, Sutter instrument, Novato, CA; RRID:SCR_021042) and
658 used for patch clamp recording with a resistance of 3–6 MOhm when filled with (1)
659 cesium methanesulfonate-based internal solution of (in mM): 120 CH_3O_3SCs, 2.8 NaCl,
660 10 HEPES, 0.4 Na_4-EGTA, 5 QX314-HBr, 5 phosphocreatine, 0.1 spermine, 4 ATP-Mg,
661 and 0.4 GTP-Na (pH 7.3, 290 mOsm); or (2) K-gluconate based internal solution,
662 containing (in mM): 140 K-gluconate, 3.8 NaCl, 1 $MgCl_2$, 10 HEPES, 0.1 Na_4-EGTA, 2
663 ATP-Mg, and 0.1 GTP-Na (pH 7.3, 290 mOsm). Optogenetic stimulation was delivered
664 using a 478 nm LED (pE-300^{Ultra}, CoolLED, UK; RRID:SCR_021972) through a 60x
665 objective lens (Olympus). Electrophysiology data were analyzed and quantified using
666 Clampfit 11.1 (Molecular Devices, San Jose, CA; RRID:SCR_011323).
667
668 *Immunohistochemistry*
669 Brain tissues after electrophysiology brain slice preparation were fixed in 4% PFA in 0.1
670 M phosphate buffer overnight at 4 °C and then were resected into 70–100 μm slices
671 using a VT1000s vibratome (Leica Biosystems, Deer Park, IL; RRID:SCR_016495) to
672 prepare brain sections for immunohistochemistry of tyrosine hydroxylase (TH). In
673 vGluT2 stereology and neuronal morphology studies, mice were perfused with ice-cold
674 phosphate-buffered saline (PBS, pH = 7.4) for 5 min and subsequently with 4% PFA
675 mice for 30 min. The brain was then extracted and saved in 4% PFA overnight at 4 °C

676 before being resected into 70 μm slices using a VT1000s vibratome (Leica Biosystems,
677 Deer Park, IL; RRID:SCR_016495) for immunohistochemistry or morphology studies.
678 Brain slices were rinsed 3x with PBS before being incubated with 0.2% Triton X-100
679 and 2% normal donkey serum (Sigma-Aldrich) for 60 min at room temperature. Brain
680 slices were then incubated with primary antibodies, including mouse anti-TH (1:2000,
681 cat# MAB318, Sigma-Aldrich; RRID:AB_2201528), or guinea pig anti-vGluT2 (cat#
682 135404, Synaptic Systems, RRID:AB_887884) for 48 hours at 4 °C or overnight at room
683 temperature. Sections were then rinsed 3x with PBS and incubated with secondary
684 antibodies for 90 min, including donkey anti-mouse Alexa Fluor 488 (Cat# 715-545-150;
685 Jackson ImmunoResearch Labs, West Grove, PA; RRID:AB_2340846), donkey anti-
686 mouse Alexa Fluor 594 (Cat# 715-585-150; Jackson ImmunoResearch Labs, West
687 Grove, PA; RRID:AB_2340854), or donkey anti-guinea pig Alexa Fluor 488 (Cat# 706-
688 545-148; Jackson ImmunoResearch Labs, West Grove, PA; RRID:AB_2340472), at
689 room temperature before washing with PBS for 3 times. Brain sections were mounted
690 with VECTASHIELD antifade mounting medium (Cat# H-1000, Vector Laboratories,
691 Newark, CA; RRID:AB_2336789), were cover-slipped and sealed with nail polish. TH-
692 and vGluT2- immunoreactivity (ir) was imaged using an Olympus DP80 camera through
693 an Olympus BX63F microscope, or a confocal laser scanning microscope (A1R, Nikon,
694 Japan; RRID:SCR_020317). TH-ir of control and 6-OHDA mice was quantified by
695 normalizing the striatal TH-ir from the ipsilateral side to the value from the contralateral
696 hemisphere, with a subtraction of background measured from the cerebral cortex.
697
698 *Animal behavior*

699 To assess parkinsonian motor deficits, mice were subject to 1) open field locomotion
700 test, where their locomotor activity and rotations were monitored for 10 min and
701 quantified using Anymaze software (Stoelting, Wood Dale, IL); (2) cylinder test using a
702 600-ml glass beaker to assess the spontaneous forelimbs use during weight-bearing
703 touches which were recorded using a digital camcorder at 60 fps (Panasonic, HC-
704 V180K) and analyzed off-line by a researcher blinded to treatments. In chemogenetic
705 studies, behavioral assessment was conducted 30 min after subcutaneous injection of
706 saline- or water-soluble clozapine-n-oxide (CNO, 1 mg/kg body weight, cat# HB6149,
707 HelloBio, Princeton, NJ).
708
709 *Confocal imaging and digital image analysis*
710 vGluT2-ir was collected from the layers 5A and 5B under a 100x objective using a Nikon A1R
711 confocal microscope. Z stack Images with a 0.15 μm interval were taken under the identical
712 settings, including laser power, gain, pinhole size, and scanning speed etc. between animals.
713 The density of vGluT2-ir was estimated based on the immunostaining signals between 5 and 8
714 μm below the surface of slices using the optical dissector method (West, 1999). For spine
715 density analysis and dendritic examination, segments of basal dendrites were tracked down
716 from the cell bodies of retrogradely labeled PT neurons in M1 and imaged under an oil-
717 immersion 100x objective using the confocal microscope (NA = 1.45; x/y, 1024 X 1024 pixels; z
718 step = 0.5 μm, A1R, Nikon). The distance from the soma to the basal dendrites analyzed was
719 50–100 μm. eGFP-labeled segments of the apical dendrites were selected from the layer I. To
720 quantify spine density and dendritic diameter, only microscopic image data with ample eGFP
721 expression and high signal-to-noise ratios were included. Spine density analysis was performed
722 using Imaris software (version 9.3, Oxford, UK; RRID:SCR_007370). Briefly, 2-3 dendritic
723 segments from the layer I and the layer V measuring 20–30 microns in length were

724 reconstructed three-dimensionally using Imaris' filament tracer function from each confocal
725 image. Spines were then manually traced, reconstructed, and quantified. For accurate three-
726 dimensionally reconstruction, both the dendrite segments and spines were recomputed
727 automatically based on the manual traces. To quantify dendritic diameter, dendritic segments
728 (30–40 μm in length) were traced and straightened using ImageJ (NIH, Bethesda, MD;
729 RRID:SCR_003070). A grid (grid type: lines with 2 μm intervals; area per point: 5 μm^2; center
730 grid on image) was placed over top of the dendritic segments and cross-sectional
731 measurements were taken along the dendrite at each grid mark (control: 240 and 262
732 measurements from 3 mice for the layer I and V, respectively; 6-OHDA: 240 and 267
733 measurements from 3 mice for the layer I and V, respectively).
734
735 *Statistics*
736 Data were collected from 3-8 mice per study. Statistics analysis was performed in GraphPad
737 Prism 9 (GraphPad Software, San Diego, CA; RRID:SCR_002798). Nonparametric Mann-
738 Whitney U (MWU) test, Wilcox signed rank (WSR) test, and Kruskal–Wallis test followed by
739 Dunn's Multiple Comparisons (as indicated in the text) were used to compare the medians of 2
740 or 3 groups in order to minimize the assumption of dataset normality. Two-way ANOVA was
741 used to compare effect of DA depletion or NMDA incubation on synaptic strength/AP firing
742 across a range of stimulation intensities followed by Šídák's multiple comparisons test. All
743 statistic tests were two tailed with p values < 0.05 (*), 0.01 (**), or 0.001 (***) as
744 thresholds for statistical significance. Data are reported as median plus interquartile ranges.

745 **Data availability.** The datasets generated during and/or analyzed during the current
746 study are available from the corresponding author on reasonable request.

747

References cited

Aeed, F., Cermak, N., Schiller, J., and Schiller, Y. (2021). Intrinsic Disruption of the M1 Cortical Network in a Mouse Model of Parkinson's Disease. Movement Disord *36*, 1565–1577. https://doi.org/10.1002/mds.28538.

Albin, R.L., Young, A.B., and Penney, J.B. (1989). The functional anatomy of basal ganglia disorders. Trends Neurosci *12*, 366–375. https://doi.org/10.1016/0166-2236(89)90074-x.

Biane, J.S., Takashima, Y., Scanziani, M., Conner, J.M., and Tuszynski, M.H. (2016). Thalamocortical Projections onto Behaviorally Relevant Neurons Exhibit Plasticity during Adult Motor Learning. Neuron *89*, 1173–1179. https://doi.org/10.1016/j.neuron.2016.02.001.

Brazhnik, E., McCoy, A.J., Novikov, N., Hatch, C.E., and Walters, J.R. (2016). Ventral Medial Thalamic Nucleus Promotes Synchronization of Increased High Beta Oscillatory Activity in the Basal Ganglia–Thalamocortical Network of the Hemiparkinsonian Rat. J Neurosci *36*, 4196–4208. https://doi.org/10.1523/jneurosci.3582-15.2016.

Brown, A.R., Hu, B., Antle, M.C., and Teskey, G.C. (2009). Neocortical movement representations are reduced and reorganized following bilateral intrastriatal 6-hydroxydopamine infusion and dopamine type-2 receptor antagonism. Exp Neurol *220*, 162–170. https://doi.org/10.1016/j.expneurol.2009.08.015.

Bruno, R.M., and Sakmann, B. (2006). Cortex Is Driven by Weak but Synchronously Active Thalamocortical Synapses. Science *312*, 1622–1627. https://doi.org/10.1126/science.1124593.

Chen, L., Daniels, S., Kim, Y., and Chu, H.-Y. (2021). Cell Type-Specific Decrease of the Intrinsic Excitability of Motor Cortical Pyramidal Neurons in Parkinsonism. J Neurosci *41*, 5553–5565. https://doi.org/10.1523/jneurosci.2694-20.2021.

Chu, H.-Y., McIver, E.L., Kovaleski, R.F., Atherton, J.F., and Bevan, M.D. (2017). Loss of hyperdirect pathway cortico-subthalamic inputs following degeneration of midbrain dopamine neurons. Neuron *95*, 1306-1318.e5. https://doi.org/10.1016/j.neuron.2017.08.038.

Cousineau, J., Lescouzères, L., Taupignon, A., Delgado-Zabalza, L., Valjent, E., Baufreton, J., and Bon-Jégo, M.L. (2020). Dopamine D2-like receptors modulate intrinsic properties and synaptic transmission of parvalbumin interneurons in the mouse primary motor cortex. Eneuro ENEURO.0081-20.2020. https://doi.org/10.1523/eneuro.0081-20.2020.

783 Galvan, A., and Wichmann, T. (2008). Pathophysiology of parkinsonism. Clin
784 Neurophysiology Official J Int Fed Clin Neurophysiology *119*, 1459–1474.
785 https://doi.org/10.1016/j.clinph.2008.03.017.

786 Gaspar, P., Duyckaerts, C., Alvarez, C., Javoy-Agid, F., and Berger, B. (1991).
787 Alterations of dopaminergic and noradrenergic innervations in motor cortex in
788 Parkinson's disease. Ann Neurol *30*, 365–374. https://doi.org/10.1002/ana.410300308.

789 Georgopoulos, A.P., and Carpenter, A.F. (2015). Coding of movements in the motor
790 cortex. Curr Opin Neurobiol *33*, 34–39. https://doi.org/10.1016/j.conb.2015.01.012.

791 Goldberg, J.A., Boraud, T., Maraton, S., Haber, S.N., Vaadia, E., and Bergman, H.
792 (2002). Enhanced synchrony among primary motor cortex neurons in the 1-Methyl-4-
793 Phenyl-1,2,3,6-Tetrahydropyridine primate model of Parkinson's disease. J Neurosci *22*,
794 4639–4653. https://doi.org/10.1523/jneurosci.22-11-04639.2002.

795 Guo, J.-Z., Graves, A.R., Guo, W.W., Zheng, J., Lee, A., Rodríguez-González, J., Li, N.,
796 Macklin, J.J., Phillips, J.W., Mensh, B.D., et al. (2015a). Cortex commands the
797 performance of skilled movement. Elife *4*, e10774. https://doi.org/10.7554/elife.10774.

798 Guo, L., Xiong, H., Kim, J.-I., Wu, Y.-W., Lalchandani, R.R., Cui, Y., Shu, Y., Xu, T., and
799 Ding, J.B. (2015b). Dynamic rewiring of neural circuits in the motor cortex in mouse
800 models of Parkinson's disease. Nat Neurosci *18*, 1299–1309.
801 https://doi.org/10.1038/nn.4082.

802 Hooks, B.M., Mao, T., Gutnisky, D.A., Yamawaki, N., Svoboda, K., and Shepherd,
803 G.M.G. (2013). Organization of Cortical and Thalamic Input to Pyramidal Neurons in
804 Mouse Motor Cortex. J Neurosci *33*, 748–760. https://doi.org/10.1523/jneurosci.4338-
805 12.2013.

806 Hyland, B.I., Seeger-Armbruster, S., Smither, R.A., and Parr-Brownlie, L.C. (2019).
807 Altered recruitment of motor cortex neuronal activity during the grasping phase of skilled
808 reaching in a chronic rat model of unilateral Parkinsonism. J Neurosci *39*, 0720–19.
809 https://doi.org/10.1523/jneurosci.0720-19.2019.

810 Kim, J., Kim, Y., Nakajima, R., Shin, A., Jeong, M., Park, A.H., Jeong, Y., Jo, S., Yang,
811 S., Park, H., et al. (2017). Inhibitory Basal Ganglia Inputs Induce Excitatory Motor
812 Signals in the Thalamus. Neuron *95*, 1181-1196.e8.
813 https://doi.org/10.1016/j.neuron.2017.08.028.

814 Kuramoto, E., Furuta, T., Nakamura, K.C., Unzai, T., Hioki, H., and Kaneko, T. (2009).
815 Two Types of Thalamocortical Projections from the Motor Thalamic Nuclei of the Rat: A
816 Single Neuron-Tracing Study Using Viral Vectors. Cereb Cortex *19*, 2065–2077.
817 https://doi.org/10.1093/cercor/bhn231.

818 Lafourcade, M., Goes, M.-S.H. van der, Vardalaki, D., Brown, N.J., Voigts, J., Yun,
819 D.H., Kim, M.E., Ku, T., and Harnett, M.T. (2022). Differential dendritic integration of
820 long-range inputs in association cortex via subcellular changes in synaptic AMPA-to-
821 NMDA receptor ratio. Neuron https://doi.org/10.1016/j.neuron.2022.01.025.

822 McColgan, P., Joubert, J., Tabrizi, S.J., and Rees, G. (2020). The human motor cortex
823 microcircuit: insights for neurodegenerative disease. Nat Rev Neurosci *21*, 401–415.
824 https://doi.org/10.1038/s41583-020-0315-1.

825 McGregor, M.M., and Nelson, A.B. (2019). Circuit mechanisms of Parkinson's disease.
826 Neuron *101*, 1042–1056. https://doi.org/10.1016/j.neuron.2019.03.004.

827 McIver, E.L., Atherton, J.F., Chu, H.-Y., Cosgrove, K.E., Kondapalli, J., Wokosin, D.,
828 Surmeier, D.J., and Bevan, M.D. (2019). Maladaptive downregulation of autonomous
829 subthalamic nucleus activity following the loss of midbrain dopamine neurons. Cell
830 Reports *28*, 992-1002.e4. https://doi.org/10.1016/j.celrep.2019.06.076.

831 Miller, O.H., Bruns, A., Ammar, I.B., Mueggler, T., and Hall, B.J. (2017). Synaptic
832 Regulation of a Thalamocortical Circuit Controls Depression-Related Behavior. Cell
833 Reports *20*, 1867–1880. https://doi.org/10.1016/j.celrep.2017.08.002.

834 Oswal, A., Brown, P., and Litvak, V. (2013). Synchronized neural oscillations and the
835 pathophysiology of Parkinson's disease. Curr Opin Neurol *26*, 662–670.
836 https://doi.org/10.1097/wco.0000000000000034.

837 Pasquereau, B., and Turner, R.S. (2011). Primary motor cortex of the parkinsonian
838 monkey: differential effects on the spontaneous activity of pyramidal tract-type neurons.
839 Cereb Cortex *21*, 1362–1378. https://doi.org/10.1093/cercor/bhq217.

840 Pasquereau, B., DeLong, M.R., and Turner, R.S. (2016). Primary motor cortex of the
841 parkinsonian monkey: altered encoding of active movement. Brain *139*, 127–143.
842 https://doi.org/10.1093/brain/awv312.

843 Petreanu, L., Huber, D., Sobczyk, A., and Svoboda, K. (2007). Channelrhodopsin-2–
844 assisted circuit mapping of long-range callosal projections. Nat Neurosci *10*, 663–668.
845 https://doi.org/10.1038/nn1891.

846 Plowman, E.K., Thomas, N.J., and Kleim, J.A. (2011). Striatal Dopamine Depletion
847 Induces Forelimb Motor Impairments and Disrupts Forelimb Movement Representations
848 within the Motor Cortex. J Park Dis *1*, 93–100. https://doi.org/10.3233/jpd-2011-11017.

849 Sauerbrei, B.A., Guo, J.-Z., Cohen, J.D., Mischiati, M., Guo, W., Kabra, M., Verma, N.,
850 Mensh, B., Branson, K., and Hantman, A.W. (2020). Cortical pattern generation during
851 dexterous movement is input-driven. Nature *577*, 386–391.
852 https://doi.org/10.1038/s41586-019-1869-9.

Shenoy, K.V., Sahani, M., and Churchland, M.M. (2012). Cortical Control of Arm Movements: A Dynamical Systems Perspective. Annu Rev Neurosci. *36*, 337–359. https://doi.org/10.1146/annurev-neuro-062111-150509.

Turrigiano, G. (2011). Too Many Cooks? Intrinsic and Synaptic Homeostatic Mechanisms in Cortical Circuit Refinement. Annu Rev Neurosci *34*, 89–103. https://doi.org/10.1146/annurev-neuro-060909-153238.

Viaro, R., Morari, M., and Franchi, G. (2011). Progressive motor cortex functional reorganization following 6-hydroxydopamine lesioning in rats. J Neurosci *31*, 4544–4554. https://doi.org/10.1523/jneurosci.5394-10.2011.

Villalba, R.M., Behnke, J.A., Pare, J.-F., and Smith, Y. (2021). Comparative Ultrastructural Analysis of Thalamocortical Innervation of the Primary Motor Cortex and Supplementary Motor Area in Control and MPTP-Treated Parkinsonian Monkeys. Cereb Cortex https://doi.org/10.1093/cercor/bhab020.

Villalobos, C.A., and Basso, M.A. (2022). Optogenetic activation of the inhibitory nigro-collicular circuit evokes contralateral orienting movements in mice. Cell Reports *39*, 110699. https://doi.org/10.1016/j.celrep.2022.110699.

Vitrac, C., and Benoit-Marand, M. (2017). Monoaminergic Modulation of Motor Cortex Function. Front Neural Circuit *11*, 72. https://doi.org/10.3389/fncir.2017.00072.

Wang, H., Stradtman, G.G., Wang, X.-J., and Gao, W.-J. (2008). A specialized NMDA receptor function in layer 5 recurrent microcircuitry of the adult rat prefrontal cortex. Proc National Acad Sci *105*, 16791–16796. https://doi.org/10.1073/pnas.0804318105.

West, M.J. (1999). Stereological methods for estimating the total number of neurons and synapses: issues of precision and bias. Trends Neurosci *22*, 51–61. https://doi.org/10.1016/s0166-2236(98)01362-9.

Wojcik, S.M., Rhee, J.S., Herzog, E., Sigler, A., Jahn, R., Takamori, S., Brose, N., and Rosenmund, C. (2004). An essential role for vesicular glutamate transporter 1 (VGLUT1) in postnatal development and control of quantal size. Proc National Acad Sci *101*, 7158–7163. https://doi.org/10.1073/pnas.0401764101.

Xu, T., Yu, X., Perlik, A.J., Tobin, W.F., Zweig, J.A., Tennant, K., Jones, T., and Zuo, Y. (2009). Rapid formation and selective stabilization of synapses for enduring motor memories. Nature *462*, 915–919. https://doi.org/10.1038/nature08389.